Materials Today Communications 56 (2026) 116235

Contents lists available at ScienceDirect

Materials Today Communications

journal homepage: www.elsevier.com/locate/mtcomm

Methanolic fruit extract of *Moringa oleifera* as a low-dose green corrosion inhibitor for carbon steel in 1M HCl: Electrochemical, surface, HPLC-DAD, and computational insights

Samra Amamra [a,b,c,*], Ilhem Kaabi [b], Hamza Behloul [a], Naouel Boussoualim [d], Farida Belkhiri [d], Khalil Kaouane [e], Hamza Kemchache [e], Abdul Ahad [f], Byong-Hun Jeon [g,**], Hyun-Jo Ahn [g], Yacine Benguerba [h,**]

[a] Department of Matter Sciences, Faculty of Sciences and Technology, University Mohamed El Bachir El-Ibrahimi, Bordj Bou Arreridj, 34000, Algeria
[b] Laboratory of Electrochemistry of Molecular Materials and Complexes (LEMMC). Department of Engineering Process, Faculty of Technology, Setif 1 University-Ferhat Abbas, Setif, 19000, Algeria
[c] Laboratory of Therapeutic Organic Substances and Sustainable Processes (LTOSSP), University of M'Sila, 28000, Algeria
[d] Department of Microbiology, Setif 1 University-Ferhat Abbas, Setif, 19000, Algeria
[e] Laboratory of Applied Biochemistry, Faculty of Nature and Life Sciences, Setif 1 University-Ferhat Abbas, Setif, 19000, Algeria
[f] Department of Pharmaceutics, College of Pharmacy, King Saud University, PO Box 2457, Riyadh, 11451, Saudi Arabia
[g] Department of Earth Resources and Environmental Engineering, Hanyang University, 222 Wangsimni-ro, Seongdong-gu, Seoul, 04763, Republic of Korea
[h] Laboratoire de Biopharmacie Et Pharmacotechnie (LPBT), Ferhat Abbas Sétif 1 University, Sétif, 19000, Algeria

ARTICLE INFO

Keywords:
Moringa oleifera
Carbon steel
Corrosion inhibition
Green inhibitor
Electrochemical impedance spectroscopy
DFT
COSMO-RS

ABSTRACT

This study evaluates the methanolic fruit extract of *Moringa oleifera* (MOME) as a green corrosion inhibitor for carbon steel in 1 M HCl. Corrosion performance was assessed by weight-loss measurements (WL), potentiodynamic polarization (PDP), and electrochemical impedance spectroscopy (EIS). At the same time, surface and compositional analyses included Atomic Force Microscopy (AFM), optical microscopy, UV-Vis spectroscopy, phytochemical screening, and High-Performance Liquid Chromatography coupled with Diode Array Detection (HPLC-DAD). The extract exhibited strong inhibition efficiency, reaching nearly 90% at 20 mg/L, and behaved as a mixed-type inhibitor. Adsorption data followed the Langmuir isotherm, indicating the formation of a protective interfacial film on the steel surface. Surface observations confirmed substantial mitigation of acid-induced damage in the presence of the extract. HPLC-DAD and phytochemical analyses revealed polyphenolic and flavonoid constituents that likely promote adsorption via oxygen-donor sites, aromatic π systems, and moderate metal-chelating ability. Density Functional Theory (DFT) and Conductor-like Screening Model for Real Solvents (COSMO-RS) analyses further supported the favorable electronic and polarity features of the major constituents, particularly rutin, quercetin, and ellagic acid, for interaction with the metal surface. Overall, the results demonstrate that *Moringa oleifera* fruit extract is an efficient, low-dose, and sustainable corrosion inhibitor for carbon steel in acidic media.

1. Introduction

Corrosion is a destructive phenomenon resulting from chemical or electrochemical interactions between metals and their surrounding environment. Its consequences are particularly severe in industrial sectors that extensively use metallic materials. Production interruptions, premature equipment failure, frequent replacement of corroded components, safety hazards, and environmental contamination are among the many adverse effects associated with corrosion, all of which impose substantial economic and societal costs. Corrosion represents a major industrial and economic challenge that affects infrastructure, transportation networks, energy production facilities, and manufacturing

* Corresponding author at: Department of Matter Sciences, Faculty of Sciences and Technology, University Mohamed El Bachir El-Ibrahimi, Bordj Bou Arreridj 34000, Algeria.
** Corresponding authors.
E-mail addresses: samra.amamra@univ-bba.dz (S. Amamra), bhjeon@hanyang.ac.kr (B.-H. Jeon), benguerbayacine@yahoo.fr (Y. Benguerba).

https://doi.org/10.1016/j.mtcomm.2026.116235
Received 25 April 2026; Received in revised form 8 September 2026; Accepted 24 September 2026
Available online 25 September 2026
2352-4928/© 2026 The Authors. Published by Elsevier Ltd. This is an open access article under the CC BY-NC-ND license (http://creativecommons.org/licenses/by-nc-nd/4.0/).

worldwide. According to NACE International, the global cost of corrosion is approximately US$2.5 trillion annually, corresponding to 3–4% of global gross domestic product (GDP). Consequently, the development of effective, sustainable, and environmentally friendly corrosion mitigation strategies remains a critical scientific and technological priority [1]. The development of efficient corrosion prevention strategies is therefore an urgent priority. Among the various methods available, corrosion inhibitors have proven highly effective in reducing or delaying the degradation of metallic materials. Inhibitors act primarily through adsorption onto the metal surface, which can occur via chemisorption (formation of coordinated covalent bonds) or physisorption (electrostatic interactions between charged inhibitor species and the metal) [2]. This adsorption process forms a uniform protective film that prevents or slows the penetration of aggressive species, such as chloride ions, thereby preserving the integrity of the metal [3].

Over the past decades, numerous organic molecules containing heteroatoms (O, N, S, P) and conjugated π-electron systems have been identified as efficient corrosion inhibitors [4–8]. Their inhibition efficiency depends on several physicochemical factors, including the type and position of functional groups, electron density at donor atoms, orbital hybridization, and the overall electronic structure of the molecule [9]. Despite their effectiveness, many synthetic inhibitors suffer from limitations such as toxicity, high production costs, and environmental persistence, which restrict their large-scale industrial application. This has motivated the scientific community to search for "green" alternatives that combine efficiency with environmental compatibility [10].

Plant-derived extracts have recently emerged as promising candidates for corrosion inhibition due to their rich phytochemical composition, natural abundance, biodegradability, and low toxicity [11,12]. These extracts contain diverse secondary metabolites—such as tannins, alkaloids, saponins, flavonoids, terpenoids, and polyphenols—with strong adsorption capacities and antioxidant properties. Their molecular structures often feature heteroatoms and aromatic systems with conjugated bonds, enabling effective interaction with metallic surfaces through electron donation and π-backbonding. Importantly, numerous studies have highlighted a close relationship between the antioxidant activity of plant extracts and their ability to act as corrosion inhibitors, as both mechanisms rely on free radical scavenging and electron-transfer processes [9].

Within this context, *Moringa oleifera* L., commonly known as the drumstick or horseradish tree, has attracted interest as a source of bioactive molecules. Native to South Asia and now widely cultivated in tropical and subtropical regions, the plant is rich in phenolic acids and flavonoids distributed across its leaves, seeds, pods, flowers, roots, and fruits. Reported constituents such as gallic, ferulic, caffeic, and chlorogenic acids, as well as quercetin, rutin, and kaempferol, exhibit antioxidant, metal-chelating, and adsorption-related properties. These characteristics make *Moringa oleifera* a relevant candidate for corrosion-inhibition studies, especially in acidic environments where steel is highly susceptible to attack.

Numerous studies have highlighted the significant potential of *Moringa oleifera* as an efficient, sustainable, and environmentally benign corrosion inhibitor (with an inhibition efficiency of more than 90%), primarily attributed to its abundance of bioactive phytochemical constituents capable of interacting with metallic surfaces and forming an adsorbed protective layer.

In particular, *Moringa oleifera* has demonstrated the ability to mitigate the corrosion of various metals and alloys. A wide range of experimental techniques has been employed to assess the corrosion inhibition efficiency (IE) of *Moringa oleifera*. These include the weight loss (WL) method, particularly for investigating the effects of exposure time and temperature, as well as electrochemical techniques such as potentiodynamic polarization (PDP) and electrochemical impedance spectroscopy (EIS). These methods provide valuable insights into the inhibition mechanism and the protective performance of the extract.

Furthermore, the protective film formed on the metallic surface has been characterized using complementary analytical techniques, including Fourier-Transform Infrared Spectroscopy (FTIR), Chromatography-Mass Spectrometry (GC-MS), UV-Visible Spectroscopy (UV-Vis), and Scanning Electron Microscopy (SEM). Collectively, these characterization methods contribute to elucidating the chemical composition, adsorption behavior, surface morphology, and corrosion inhibition mechanism of *Moringa oleifera* [13–18].

Furthermore, the scientific novelty of the present investigation resides in the synergistic integration of *Moringa oleifera* fruit extract as a bio-based corrosion inhibitor at low concentration with advanced computational approaches, namely Density Functional Theory (DFT) and COSMO-RS analyses. This combined experimental–molecular-level calculations strategy enables a more rigorous elucidation of the adsorption behavior, active molecular sites, intermolecular interactions, and inhibition mechanism of the bioactive constituents present in the fruit extract.

In light of the foregoing, the present study investigates the methanolic extract of *Moringa oleifera* fruits (MOME) as a low-dose green inhibitor for carbon steel in hydrochloric acid. Corrosion performance was evaluated using gravimetric analysis, potentiodynamic polarization, and electrochemical impedance spectroscopy. HPLC-DAD profiling and phytochemical screening were used to identify the major active constituents. In contrast, AFM, optical microscopy, UV-Vis analysis, and adsorption isotherm modeling were used to clarify the inhibition mechanism. Antioxidant assays were included as supporting evidence for the extract's redox activity. At the same time, computational analyses were used to evaluate the intrinsic electronic properties and reactivity descriptors of the dominant polyphenolic compounds.

Overall, this work contributes to the development of environmentally friendly corrosion inhibitors by demonstrating that *Moringa oleifera* fruit extract can provide efficient protection at low dosage. The study aligns with the principles of green chemistry and sustainable materials protection. It provides a coherent experimental and theoretical basis for further optimization of plant-derived inhibitors for the control of acidic corrosion.

2. Materials and methods

2.1. Materials

Analytical grade reagents were used: Folin–Ciocalteu reagent, gallic acid, aluminum chloride, quercetin, Dragendorff reagent, Stiasny reagent, methanol, hydrochloric acid (HCl), ammonium hydroxide (NH_4OH), sulfuric acid (H_2SO_4), dimethyl sulfoxide (DMSO), and 2,2-diphenyl-1-picrylhydrazyl (DPPH). Ultrapure water was used in all preparations. Instrumentation comprised a UV–Vis spectrophotometer, a PGZ 301 Voltalab 40 potentiostat controlled by VoltaMaster 4, and a three-electrode electrochemical cell with carbon steel X48 as the working electrode, graphite as the counter electrode, and a saturated calomel reference electrode (Hg, Hg_2Cl_2, KCl). A rotary evaporator was used for solvent removal. High-performance liquid chromatography (HPLC) was performed on an Agilent 1260 system. Atomic force microscopy (AFM) images were obtained using an Oxford Instruments microscope.

2.2. Plant material and authentication

Moringa oleifera fruits (Fig. 1) were collected in October 2023 from Noumirat, Ghardaïa, southern Algeria. Botanical identification was verified by Prof. Hocine Laouer (Ferhat Abbas University, Setif, Algeria). Fruits were shade-dried at ambient temperature, then ground to a fine powder to increase the extraction surface area.



Fig. 1. Photo of *Moringa oleifera* fruit.

2.3. Extract characterization

2.3.1. Phytochemical Screening

Qualitative screening followed Bruneton to identify major classes of bioactives, including alkaloids, tannins, coumarins, flavonoids, mucilage, and saponins [19].

2.3.2. Extraction procedure

Following Markham et al. [20], 500 g of powdered fruits were macerated with 1000 mL of methanol at room temperature for 5 days. The mixture was filtered through Whatman paper, and the solvent was removed under reduced pressure at 40 °C using a BÜCHI rotary evaporator. The residue was designated *Moringa oleifera* methanolic extract (MOME).

2.3.3. Total phenolic and flavonoid contents

The Folin determined total phenolic content (TPC)–Ciocalteu method [21]. An aliquot of 50 µL extract was mixed with 250 µL Folin–Ciocalteu reagent (2 M, diluted 1:10) and 250 µL sodium carbonate solution (7.5 g per 100 mL). After 90 min at room temperature, absorbance was read at 756 nm. A gallic acid calibration curve was used, and results were expressed as µg gallic acid equivalents per mg dry extract (µg GAE per mg). Total flavonoid content (TFC) was measured by the aluminum chloride colorimetric method as described by Bahorun et al. [22]. One milliliter of a 2% $AlCl_3$ solution was added to 1 mL of the methanol extract. After 10 min at room temperature, absorbance was read at 430 nm. Quantification used a quercetin standard curve (0–40 mg/mL). Results were expressed as µg quercetin equivalents per mg dry extract (µg QE per mg).

2.3.4. HPLC-DAD analysis

HPLC-DAD profiling was performed on an Agilent 1260 with multiwavelength detection using a Zorbax Eclipse Plus C8 column (4.6 by 250 mm, 5 µm). Mobile phase A was water, and mobile phase B was acetonitrile containing 0.05% trifluoroacetic acid. Flow rate was 0.9 mL/min. The linear gradient was: 0 min, 82% A; 0–1 min, 82% A; 1–11 min, 75% A; 11–18 min, 60% A; 18–22 min, 82% A; 22–24 min, 82% A. Detection was at 280 nm, injection volume 5 µL, column temperature 40 °C.

2.4. Antioxidant activity

2.4.1. DPPH radical scavenging

DPPH scavenging was assessed as in [23]. Briefly, 50 µL of the extract at various concentrations was mixed with 1250 µL of DPPH in methanol (0.004%) and incubated in the dark at room temperature for 30 min. Absorbance was measured at 517 nm. Radical inhibition % was calculated as:

$$I\% = \frac{(A_{blank} - A_{extract})}{A_{blank}} \times 100 \quad (1)$$

A_{blank} is the absorbance of DPPH without extract, $A_{extract}$ is the absorbance with extract.

2.4.2. Hydroxyl radical scavenging

Hydroxyl radical scavenging was performed as described by Yang et al. with minor modifications [24]. A total of 150 µL MOME or ascorbic acid was added to 300 µL stock solution containing 9 mM $FeSO_4$ and 0.3% H_2O_2. After 15 min at 32 °C, 75 µL of 20 mM salicylic acid was added, and the mixture was incubated for another 15 min at 32 °C. Absorbance was read at 562 nm. Scavenging % was:

$$Scavenging\ effect \quad \% = \frac{(A_C - A_e)}{A_C} \times 100 \quad (2)$$

Where A_C is the control absorbance, and A_e is the absorbance with extract. IC_{50} was obtained from the dose–response curve.

2.4.3. Ferrous ion chelation

Ferrous ion chelation followed Le et al. with slight modifications [25]. A total of 0.25 mL extract at different concentrations was mixed with 0.45 mL methanol, then 0.05 mL $FeCl_3$ (0.6 mM). After 5 min, 0.05 mL ferrozine (1 mM) was added, and the mixture was incubated for 10 min at room temperature. Absorbance was read at 562 nm. Chelation % was:

$$\%\ \ inhibition = \frac{(A_0 - A_1)}{A_0} \times 100 \quad (3)$$

Where A_0 is the control absorbance, and A_1 is the absorbance with extract. Lower absorbance indicates higher chelation. IC_{50} was derived from the dose–response curve.

2.5. Antimicrobial activity

2.5.1. Antifungal assay

Antifungal activity of MOME was tested against seven clinical strains, namely Aspergillus flavus, Alternaria sp., Fusarium sp., Rhizopus sp., Penicillium sp., Candida albicans, and Fusarium oxysporum. Strains were reactivated on potato dextrose agar at 28 °C for 7 days. Inocula were prepared in sterile physiological saline. PDA plates were inoculated within 15 min using a sterile swab with four vertical passes, rotating the plate by 60 ° between passes. Sterile 6-mm paper discs were placed on the inoculated agar and loaded with 20 µL of MOME (200 mg/mL in DMSO). Discs loaded with 20 µL DMSO served as negative controls. Plates were incubated at 28 °C for 48 h, and inhibition zones were measured as diameters in millimeters [26].

2.5.2. Antibacterial assay

Antibacterial activity was evaluated by disc diffusion. Bacterial strains were streaked onto Mueller–Hinton agar and incubated at 37 °C for 24 h [27]. Colonies were suspended in sterile saline and adjusted to 0.5 McFarland (approximately 1.5×10^8 CFU per mL) [28]. Plates were swabbed uniformly in three passes with 60-degree rotations and a final pass along the plate edge. Seeded plates were held at 4 °C for 2 h to allow diffusion. Sterile 6 mm discs were loaded with 20 µL MOME (200 mg per mL in DMSO). Antibiotic discs (spiramycin, gentamicin, or cefazolin) were positive controls, and DMSO discs were negative controls. Plates were incubated at 37 °C for 24 h, and inhibition halos were measured as the mean of two perpendicular diameters through the disc center [26].

2.6. Corrosion inhibition studies

2.6.1. Metal, surface preparation, and test media

Carbon steel composition (wt%): C 0.50–0.52, Mn 0.50–0.80, Si 0.40, P less than or equal to 0.035, S less than or equal to 0.035, balance Fe. Before testing, surfaces were polished sequentially with SiC papers (80, 500, 800, 1200, 2000, 2500, 4000 grit), rinsed with distilled water, degreased with acetone, and dried. The corrosive medium used throughout the study was 1 M HCl. *Moringa oleifera* methanolic extract (MOME) was added at concentrations of 5, 7.5, 10, 12.5, 17.5, and 20 mg L^{-1} . Fresh solutions were prepared for each experiment. Fresh solutions were prepared for each experiment.

2.6.2. Weight loss measurements

Cylindrical coupons (3.5 by 1.5 cm) were polished at 350 rpm, rinsed, degreased, dried, and weighed to ±0.0001 g. Each coupon was immersed at a fixed inclination in 80 mL of electrolyte for 24 h under aerated, static conditions. After exposure, coupons were rinsed with bidistilled water and acetone, dried, and reweighed. The corrosion rate W (mg/cm^2/h) equals the mass loss divided by the exposed area and the immersion time. Inhibition efficiency

2.6.3. Electrochemical measurements

Electrochemical tests were performed at room temperature in a double-walled 100 mL Pyrex cell using a three-electrode configuration: a SCE reference electrode, a graphite counter electrode, and a carbon steel working electrode with an exposed area of 0.196 cm^2. After 45 min of open circuit stabilization, potentiodynamic polarization curves were recorded from −800 to −200 mV vs SCE at 0.5 mV per s. Electrochemical impedance spectroscopy was carried out after 30 min immersion at open circuit with a 10 mV sinusoidal perturbation over 100 kHz to 10 mHz, 10 points per decade. Data analysis was performed with VoltaMaster 4.

2.7. Molecular docking

2.7.1. Ligands and protein targets

Molecular docking was performed as a complementary approach to investigate the potential antioxidant interactions of the major phytochemicals identified in MOME. It should be emphasized that the docking analysis was not intended to model the adsorption of inhibitor molecules onto the steel surface, which is the primary mechanism governing corrosion inhibition. The corrosion inhibition behavior was instead interpreted using electrochemical measurements, adsorption studies, surface characterization, and quantum-chemical calculations (DFT and COSMO-RS). The docking study was included to provide additional insight into the extract's antioxidant properties, which may indirectly contribute to corrosion protection by mitigating oxidative processes. Three antioxidant-related enzymes were selected as biological targets: superoxide dismutase (PDB ID: 1CB4), catalase compound II (PDB ID: 2CAG), and human glutathione peroxidase 7 (PDB ID: 2P31). In addition, a protein from Acidithiobacillus ferrooxidans (PDB ID: 1H1O; resolution: 2.13 Å) was included to explore possible interactions with a microorganism associated with metal oxidation processes. Fourteen ligands tentatively identified by HPLC-DAD analysis were investigated, namely caffeic acid, chlorogenic acid, cinnamic acid, p-coumaric acid, ellagic acid, ferulic acid, gallic acid, hesperetin, quercetin, rosmarinic acid, rutin, syringic acid, vanillin, and ascorbic acid as a reference compound [29].

2.7.2. Preparation and docking protocol

Ligands were energy-minimized in Chem3D. Protein structures were prepared with Discovery Studio by removing water and nonessential heteroatoms, adding polar hydrogens, and assigning Kollman charges [30]. Docking was performed using AutoDock Vina with a $40 \times 40 \times 40$ $Å^3$ grid box centered on the active site. Multiple poses were generated for each ligand. Binding affinity and key interactions were analyzed to evaluate relative stability and to inform structure-activity interpretation.

2.8. Computational methodology

The molecular geometries of ellagic acid, quercetin, and rutin were optimized in the gas phase using Density Functional Theory (DFT) as implemented in the DMol³ code. The Becke–Lee–Yang–Parr exchange–correlation functional (B3LYP) was employed together with the double numerical basis set including polarization functions (DNP). All electrons were treated explicitly; no pseudopotentials were used, and Fermi population smearing was applied to facilitate self-consistent field convergence. The integration grid was set to medium precision, and total energy, maximum gradient, and atom displacement convergence criteria were set to 2.0×10^{-5} Ha, 4.0×10^{-3} Ha $Å^{-1}$, and 5.0×10^{-3} Å, respectively. Geometry optimization proceeded without symmetry constraints.

For solvation-related polarity analysis, COSMO calculations were performed to obtain surface charge density distributions σ(r) for each molecule. The dielectric constant was set to 78.54 to approximate aqueous conditions. The COSMO output files were then used to derive σ-profiles, which represent the probability distribution of surface charges and describe the balance between hydrogen-bond donor and acceptor regions and hydrophobic domains.

3. Results and discussion

3.1. Extraction yield

The extraction yield of the methanolic extract of *Moringa oleifera* fruits (MOME) was determined according to Eq. (4).

$$R = \frac{m_{extract}}{m_{plant\ powder}} \times 100 \quad (4)$$

where $m_{extract}$ is the mass of the dried extract and $m_{plant\ powdre}$ is the mass of the initial plant material. A yield of 2.40% was obtained. Such a moderate yield is typical for fruit matrices rich in secondary metabolites but poor in lipids. The yield can also be influenced by solvent polarity, extraction duration, particle size, and plant maturity stage [31], indicating that methanol is appropriate for recovering phenolic constituents from *Moringa* fruits.

3.2. Phytochemical screening

Preliminary phytochemical tests confirmed the presence of tannins, alkaloids, and flavonoids, while saponins were absent (Table 1). These compound classes are known to contain heteroatoms (O, N) and aromatic systems that can adsorb onto metal surfaces via electron donation, hydrogen bonding, and π-electron interactions. Their presence suggests that MOME could act as an efficient corrosion inhibitor in acidic media.

Although the cyanidin reaction produced a weak or negative

Table 1
Results of the phytochemical Screening.

		Results	
		Coloration or Precipitation	Interpretation
Alkaloids	Dragendorff's reagent	Precipitate	+++
Tannins	1% $FeCl_3$	Blue-black color	++
Flavonoids	H_2SO_4 10%, NH_4OH	Color change	-
	cyanidine reaction	negative reaction	
Saponins	distilled water	Foam	-

(- No presence/ + Less presence/ ++ Moderate presence/ +++ High presence).

response, HPLC-DAD analysis subsequently revealed the presence of several flavonoids, including rutin, quercetin, and hesperetin. This apparent discrepancy may be attributed to the limited sensitivity of qualitative phytochemical screening tests, which depend on both flavonoid concentration and structural features. In particular, glycosylated flavonoids may exhibit weaker colorimetric reactions than their aglycone counterparts. Therefore, the HPLC-DAD results provide more reliable evidence for the presence of flavonoid constituents in the extract.

3.3. Qualitative HPLC-DAD analysis results

HPLC-DAD analysis allowed tentative identification of major phenolic and flavonoid constituents by retention-time comparison with authentic standards [32]. Catechin, methyl gallate, naringenin, daidzein, and kaempferol were not detected. In contrast, several phenolic acids, namely gallic, caffeic, ferulic, syringic, p-coumaric, cinnamic, and ellagic acids, as well as the flavonoids rutin, quercetin, and hesperetin, were tentatively identified (Figs. 2 and 3).

These compounds are structurally characterized by:

- Aromatic rings, enabling π-adsorption on the steel surface.
- Multiple hydroxyl groups provide binding sites for Fe^{2+} coordination and radical quenching.

This composition suggests a strong correlation between phytochemistry, antioxidant capacity, and corrosion inhibition performance (Fig. 4).

3.4. Dosage of polyphenols and flavonoids

The total phenolic and flavonoid contents of MOME were found to be:

- TPC: 9.194 ± 0.312 µg GAE/mg extract
- TFC: 5.337 ± 0.772 µg QE/mg extract

These values reflect the presence of hydroxybenzoic, hydroxycinnamic, and flavonoid acids detected by HPLC. Environmental conditions and extraction parameters influence the quantities [33]. Since these compounds are known radical scavengers and surface-active molecules, their presence is key to both antioxidant and anticorrosion behavior.

3.5. Antioxidant activity

3.5.1. DPPH assay

The DPPH assay evaluates a compound's ability to neutralize the stable free radical 2,2′-diphenyl-1-picrylhydrazyl ($DPPH^{\bullet}$) via hydrogen-atom or electron donation. Upon reduction, $DPPH^{\bullet}$ is converted to its non-radical form (DPPH-H), resulting in a measurable decrease in absorbance at 517 nm. The magnitude of this decrease reflects the radical scavenging strength of the tested sample. Fig. 5 shows that the inhibition percentage increases progressively with increasing extract concentration, indicating a dose-dependent radical-scavenging response for MOME and the reference antioxidants. The antioxidant capacity was quantified as IC_{50}, the concentration of the sample required to neutralize 50% of DPPH radicals. Lower IC_{50} values are associated with stronger antioxidant performance [34]. In this study, ascorbic acid ($IC_{50} = 5.487 \pm 0.0003$ µg per mL) and gallic acid ($IC_{50} = 7.332 \pm 0.0009$ µg per mL) demonstrated very high radical scavenging efficiency, whereas MOME exhibited a significantly higher IC_{50} value (400.618 ± 44.006 µg per mL). This indicates that although MOME possesses antioxidant activity, its radical-quenching ability is considerably weaker than that of the pure reference compounds.

This difference is expected for two main reasons. First, plant extracts contain complex mixtures of compounds, many of which are not redox-active. Second, the concentration of phenolics within the crude extract is lower than in isolated standards. Nonetheless, the scavenging effect observed for MOME confirms that the phenolic and flavonoid constituents identified by HPLC contribute to electron and hydrogen donation processes. The relationship between polyphenol content and antioxidant behavior is not solely quantitative. Although some studies report a proportional correlation between total phenolic content and antioxidant activity, others find no direct linear relationship [34,35]. This inconsistency is explained by the fact that antioxidant efficiency is fundamentally structure-dependent. The number, position, and orientation of hydroxyl groups strongly influence the ability of phenolics to stabilize radical species [36]. Hydroxyl substituents on aromatic rings can donate hydrogen atoms to terminate radical chain reactions, while remaining resonance-stabilized themselves [37]. Compounds containing ortho-dihydroxyl (catechol) arrangements on the B-ring, conjugation between the A and B rings, or carbonyl and hydroxyl groups on the C-ring are generally more potent radical scavengers [38]. In addition, glycosylation, methoxyl substitution, and polymerization state can either enhance or diminish reactivity by altering electron density and steric accessibility [39].

Therefore, the antioxidant capacity of MOME should be interpreted

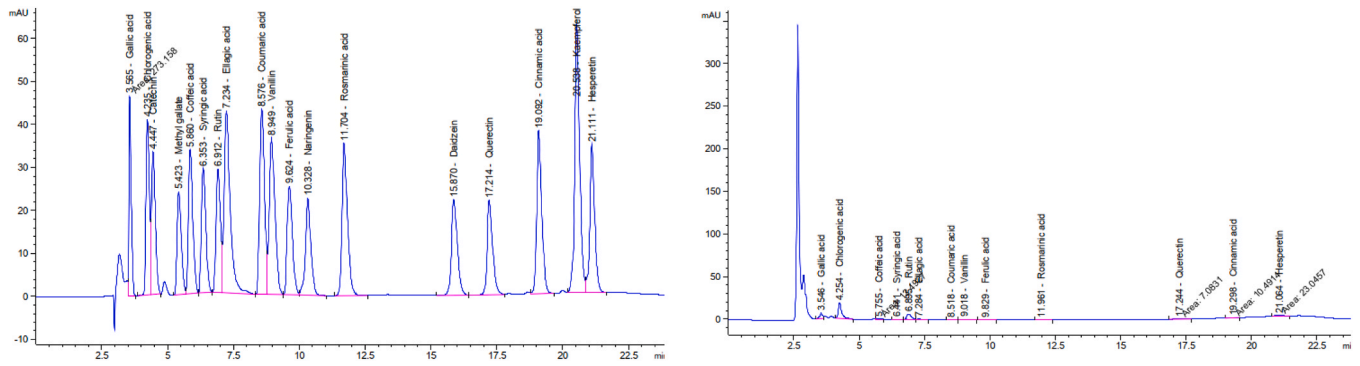

Fig. 2. HPLC-DAD analysis results.

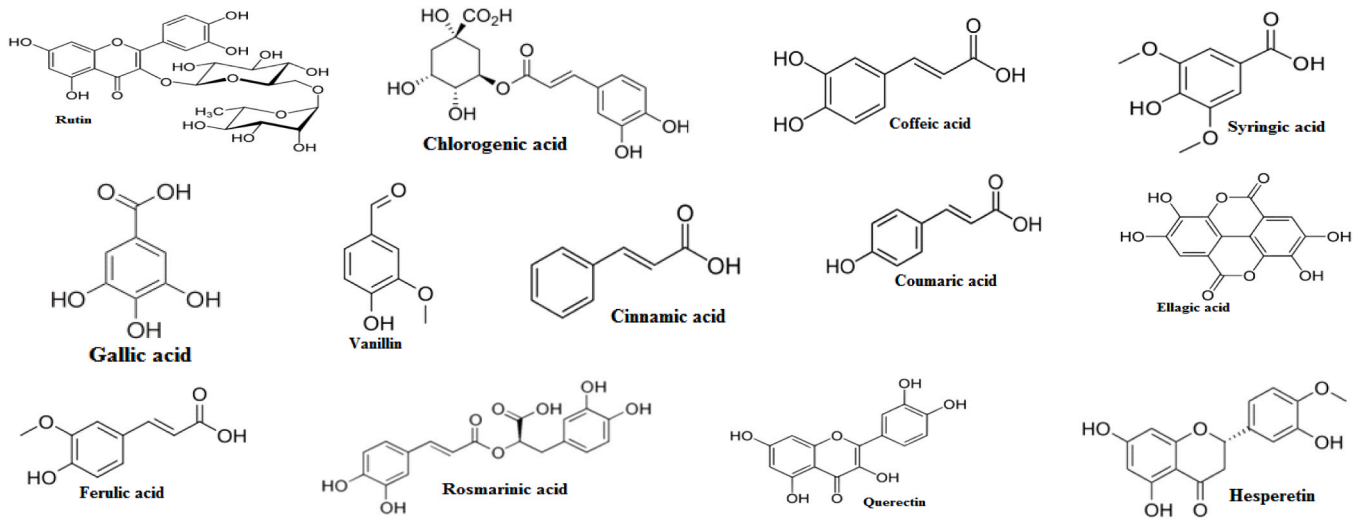

Fig. 3. Chemical structures of phenolic compounds positively identified by HPLC-DAD.

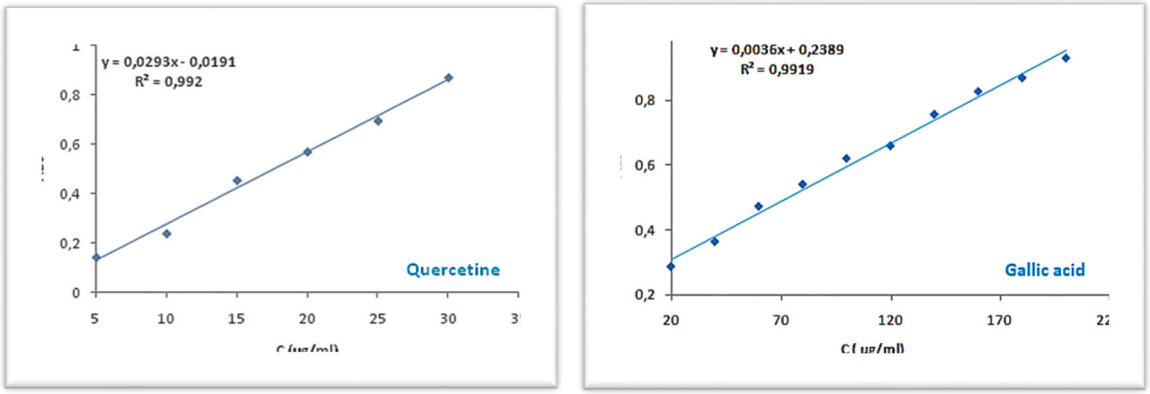

Fig. 4. Gallic acid and quercetin calibration curves.

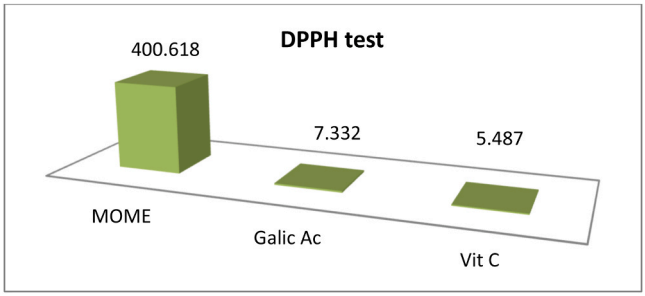

Fig. 5. IC_{50} of *Moringa oleifera* methanolic extract, gallic acid, and vitamin C determined by DPPH test.

as the combined result of multiple coexisting molecular factors: (i) the chemical identity of the dominant phenolic species, (ii) the number and reactivity of hydroxyl groups on each molecule, (iii) the degree of conjugation across the aromatic systems, and (iv) the physical interactions among phenolics in a multicomponent matrix. The moderate antioxidant activity observed is thus consistent with the extract's structural complexity. It does not diminish its relevance for corrosion inhibition, where adsorption and surface coordination, rather than radical scavenging strength alone, play the decisive role.

3.5.2. *Hydroxyl radical scavenging*

The hydroxyl radical (•OH) is recognized as one of the most reactive and short-lived oxygen-derived species in biological and chemical systems. Although structurally the neutral counterpart of the hydroxide ion (OH^-), •OH exhibits a far greater oxidative potential, enabling it to react almost instantaneously with nearby molecules. This extremely high reactivity allows •OH to initiate lipid peroxidation, disrupt protein structure, and induce oxidative DNA damage, contributing to cellular dysfunction and pathological processes [40]. For this reason, the capacity of natural compounds to neutralize •OH is considered one of the most relevant indicators of antioxidant functionality. The hydroxyl radical scavenging activity of MOME was therefore evaluated, and the results revealed a clear dose–response relationship, with the scavenging percentage increasing with increasing extract concentration. This increase confirms that the phytoconstituents in MOME can interact with and neutralize highly reactive radical species. The antioxidant capacity was expressed as IC_{50}, the concentration required to quench 50% of hydroxyl radicals [41]. MOME exhibited an IC_{50} value of 1.722 ± 0.37 mg per mL.

In contrast, ascorbic acid, used as a reference antioxidant, showed an IC_{50} value of 0.114 ± 0.004 mg/mL (Fig. 6), reflecting its superior radical-scavenging efficiency. Although MOME is significantly less potent than ascorbic acid, this does not diminish the relevance of its activity. Unlike purified ascorbic acid, the extract represents a complex mixture of bioactive molecules, including phenolic acids and flavonoids, each contributing to the overall scavenging effect. The radical

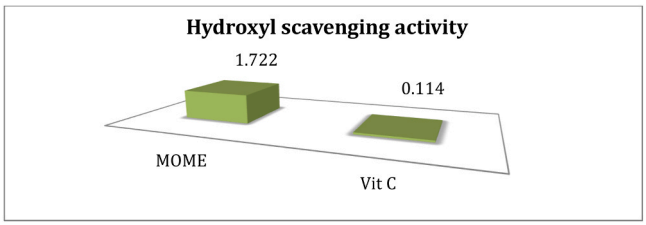

Fig. 6. IC_{50} of *Moringa oleifera* methanolic extract and vitamin C determined by the hydroxyl scavenging method.

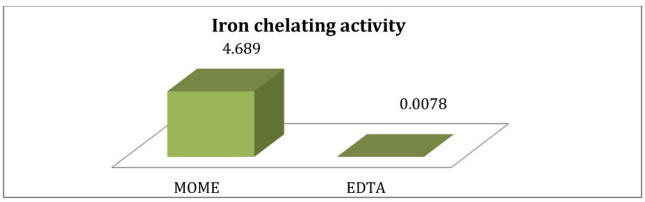

Fig. 7. IC_{50} of *Moringa oleifera* methanolic extract and EDTA determined by the iron chelating test.

neutralization mechanism here is most likely mediated by:

1. Hydrogen atom transfer (HAT) from phenolic hydroxyl groups, leading to radical stabilization.
2. Electron transfer (ET) to reduce •OH to a less reactive species.
3. Possible chelation of Fe^{2+} ions, reducing the Fenton reaction that generates hydroxyl radicals in solution.

The relatively moderate IC_{50} value, therefore, reflects the combined, synergistic action of multiple constituents rather than that of a single dominant antioxidant molecule. Additionally, the spatial arrangement and resonance stabilization of hydroxyl groups in flavonoid structures enhance their ability to delocalize unpaired electrons, thereby stabilizing the resulting phenoxyl radicals.

In this context, MOME's hydroxyl radical-scavenging capacity aligns with its phenolic composition and supports its role in mitigating oxidative processes associated with corrosion. Since hydroxyl radicals accelerate the dissolution of iron in acidic environments, the capacity of MOME to scavenge •OH may contribute to slowing down corrosion propagation at the steel surface. Thus, the antioxidant activity observed here is not only biologically relevant but also chemically aligned with the corrosion inhibition mechanism proposed in later sections.

3.5.3. Iron chelating activity

Iron plays a central role in numerous physiological functions, including oxygen transport, mitochondrial respiration, and regulation of enzymatic pathways. However, because of its high redox activity, free iron can readily cycle between Fe^{2+} and Fe^{3+} states, catalyzing the formation of reactive oxygen species (ROS). Through Fenton and Haber–Weiss reactions, excess Fe^{2+} reacts with hydrogen peroxide to generate hydroxyl radicals, which are among the most damaging oxidative species [42]. This process contributes to oxidative stress and has been linked to the progression of chronic disorders such as cancer, cardiovascular disease, neurodegeneration, and diabetes. Therefore, the ability of natural products to chelate Fe^{2+} and prevent such redox cycling is considered a key indicator of antioxidant potential.

In this study, the ferrozine assay was used to evaluate the Fe^{2+} chelation capacity of MOME. Ferrozine forms a stable, intensely colored complex with Fe^{2+}, and any reduction in absorbance indicates interference with this complex formation due to competitive chelation. Both MOME and the reference standard EDTA disrupted the formation of the ferrous–ferrozine complex, confirming the extract's ability to bind Fe^{2+} ions. This chelating effect is primarily attributed to polyphenolic and flavonoid constituents, which contain electron-rich oxygen donors capable of coordinating transition metals. MOME exhibited measurable chelating activity, with an IC_{50} value of 4.689 ± 0.106 mg/mL. As expected, EDTA displayed a much stronger affinity for Fe^{2+}, with an IC_{50} of 0.0078 ± 0.0004 mg/mL (Fig. 7), reflecting its role as a potent synthetic chelating agent. Although the chelating efficiency of MOME is considerably lower, this difference reflects the contrast between a complex plant extract and a pure, highly specialized ligand. The significance of MOME lies not in matching EDTA's chelating strength, but in providing moderate metal-binding properties alongside radical-scavenging properties within a natural, biocompatible matrix. Moreover, Fe^{2+} chelation is directly relevant to corrosion inhibition in acidic media. By binding Fe^{2+} ions near the steel surface, MOME can interfere with the dissolution–reprecipitation cycle of iron and suppress the regeneration of catalytic species that accelerate corrosion.

In other words, chelation contributes to corrosion protection by:

1. Reducing the concentration of free Fe^{2+} available for redox cycling,
2. Limiting the formation of •OH through Fenton reactions,
3. Stabilizing the interfacial environment at the metal–solution boundary.

Thus, while MOME is weaker than EDTA in terms of pure chelation, its combined radical scavenging and moderate Fe^{2+} binding capacity suggest a complementary antioxidant contribution to corrosion protection. This synergy supports its role as a naturally derived anticorrosive agent, consistent with its phytochemical composition and the electrochemical behavior discussed in later sections.

3.6. Antimicrobial activity

The antimicrobial properties of the *Moringa oleifera* methanolic extract (MOME) were evaluated against fungal species, yeasts, and nine bacterial strains selected for their clinical relevance and multidrug resistance profiles. The extract showed no antifungal activity, as no inhibition zones were detected. This absence of activity suggests that either antifungal constituents are not present in MOME or are present at levels below the threshold required to inhibit fungal growth under the conditions applied.

Regarding antibacterial activity, the extract demonstrated only weak inhibitory effects. As shown in Table 2, inhibition zones produced by MOME were very small (generally $\leq$ 12 mm) or completely absent for several strains.

In contrast, the reference antibiotics gentamicin and spiramycin produced pronounced inhibitory halos, reflecting high antibacterial efficacy. The limited antibacterial response may be attributed to the low concentration of antibacterial phytochemicals in the crude extract, restricted diffusion of active compounds through the agar matrix, or the intrinsic resistance mechanisms present in the tested bacterial strains. These results demonstrate that MOME does not exert significant antimicrobial effects under the tested conditions. Importantly, this finding clarifies that the later-observed corrosion inhibition performance is not due to microbial suppression but arises from direct chemical interactions

Table 2
Zones of inhibition (ZI, mm).

Strain	MOME	Gentamicin	Spiramycin
Klebsiella sp.	12/10	16	22
Streptococcus sp.	8/8	20	20
Klebsiella pneumoniae ATCC 13883	8/9	16	19
Salmonella typhimurium ATCC 14028	11/10	15	27
Escherichia coli ATCC 8739	–	17	8
Staphylococcus aureus ATCC 6538	–	17	22
Bacillus subtilis ATCC 6633	–	25	27
Staphylococcus aureus ATCC 25923	–	27	20
Enterobacter faecalis ATCC 29212	10/11	–	9

between phytochemicals and the metal surface. This distinction is essential for the accurate interpretation of the inhibition mechanism.

3.7. Corrosion inhibition performance

3.7.1. Weight loss measurements

The corrosion rate of carbon steel in 1 M HCl in the absence and presence of different concentrations of MOME was evaluated by gravimetric analysis. The corrosion rate (W) was calculated using Eq. (5), and the inhibition efficiency (IE%) was determined using Eq. (6):

$$W = \frac{\Delta m}{(s \times t)} \quad (5)$$

$$IE(\%) = \frac{(W_0 - W_i)}{W_0} \times 100 \quad (6)$$

Where Δm is the mass loss (mg), S is the exposed surface area (cm^2), t is the immersion time (h), W_o is the corrosion rate in the absence of inhibitor, and W_i is the corrosion rate in the presence of inhibitor.

The results in Table 3 show that the corrosion rate decreased significantly with increasing MOME concentration, accompanied by a corresponding increase in inhibition efficiency.

At the highest concentration (20 mg L^{-1}), the extract achieved an inhibition efficiency of 88.24%, demonstrating its strong ability to reduce the acid-induced dissolution of carbon steel. These trends are illustrated in Fig. 8, which shows the progressive increase in inhibition efficiency with increasing inhibitor concentration.

This behavior indicates that the phytochemical constituents of MOME adsorb onto the steel surface, forming partial coverage that limits chloride penetration and decreases the availability of active corrosion sites. A particularly noticeable increase in surface coverage was observed between 7.5 and 10 mg L^{-1} , where the surface coverage parameter (θ) increased from 0.566 to 0.851. This abrupt improvement may indicate the attainment of a critical surface coverage threshold, beyond which the adsorbed phytochemical species provide more continuous and effective protection of the steel surface. At lower concentrations, incomplete adsorption may leave a significant fraction of active sites exposed to the corrosive medium. As the inhibitor concentration increases, the adsorbed layer becomes more effective in isolating the metal surface from the electrolyte. Changes in the organization, packing density, and cooperative interactions of the adsorbed phytochemical species may also contribute to this transition, resulting in the formation of a more coherent and protective adsorbed layer. The presence of aromatic rings and electronegative functional groups (hydroxyl and carbonyl) in phenolic and flavonoid compounds enhances their adsorption propensity through electron donation and coordination interactions with the metal surface, contributing to interfacial stabilization.

Additionally, hydrogen bonding and intermolecular interactions likely promote the formation of a compact, cohesive film. The progressive increase in inhibition efficiency with concentration supports a surface coverage behavior, consistent with adsorption characteristics described by the Langmuir isotherm. Accordingly, the weight loss results

Table 3
Corrosion parameters of carbon steel in 1 M HCl solution without and with varying concentrations of MOME, determined by gravimetric measurements at 25 °C after 24 h.

Cm (mg/L)	Δm (mg)	W (mg/cm^2.h)	θ	IEw(%)
Blank	1.9769 ± 0.016	0.002305	-	-
5	0.8793 ± 0.012	0.001025	0.5553	55.53
7.5	0.8586 ± 0.024	0.001001	0.5657	56.57
10	0.2946 ± 0.011	0.000343	0.8511	85.11
12.5	0.2625 ± 0.0025	0.000306	0.8672	86.72
17.5	0.2435 ± 0.002	0.000283	0.8768	87.68
20	0.2325 ± 0.003	0.000271	0.8824	88.24

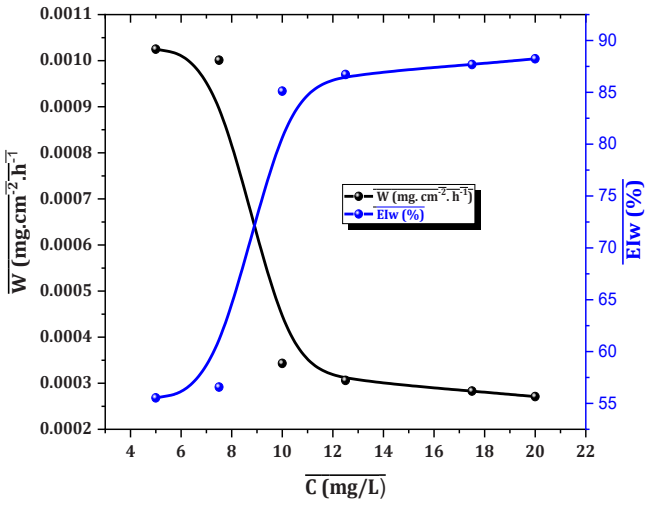

Fig. 8. Variation of inhibition efficiency and corrosion rate with different concentrations of MOME in 1 M HCl at 25 °C.

indicate that MOME acts as an effective corrosion inhibitor by reducing the active surface area available for corrosion reactions and limiting the access of aggressive species at the metal–solution interface.

3.7.2. Electrochemical study

3.7.2.1. Open circuit potential (OCP) measurements. The evolution of the open-circuit potential (OCP) reflects the establishment of interfacial electrochemical equilibrium between the steel surface and the acidic medium, as well as the effect of the inhibitor on this equilibrium. In the uninhibited 1 M HCl solution, carbon steel quickly stabilizes at a markedly negative potential, indicating rapid dissolution of iron and active hydrogen evolution. This response is typical of low-alloy steels in strong acidic media and confirms the surface's high susceptibility to electrochemical attack. When MOME is introduced, the OCP shifts toward less negative values, and the magnitude of this shift increases progressively with inhibitor concentration, as shown in Fig. 9. The shift remains below 85 mV relative to the blank, which, according to the criteria proposed in [43,44], confirms that MOME does not act exclusively on either the anodic reaction (iron oxidation) or the cathodic reaction (hydrogen evolution). Instead, the inhibitor simultaneously influences both reactions, resulting in mixed-type inhibition. This means the inhibitor reduces the overall number of electronically accessible sites

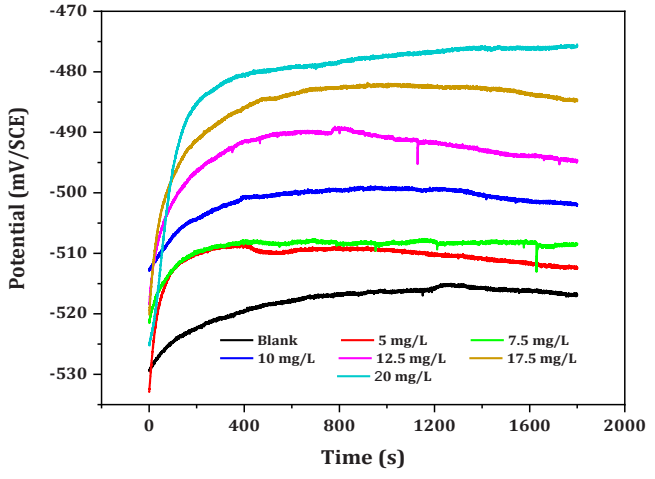

Fig. 9. Graph of open circuit potential for carbon steel in 1 M HCl solution without and with different concentrations of MOME at 25°C.

on the electrode surface rather than altering the intrinsic reaction pathways. The slight positive displacement of the potential and its rapid stabilization in the presence of MOME indicate that phytochemical constituents in the extract rapidly adsorb onto the metal interface and form a protective film. Phenolic compounds contain functional groups capable of interacting with metal surfaces via electron donation and coordination.

These molecular species can anchor via lone-pair donation or partial π-orbital interactions, thereby reducing the effective electrochemical reaction area. This adsorption pattern aligns with the decrease in mass loss (Table 3) and increase in inhibition efficiency (Fig. 8), confirming that corrosion mitigation occurs through surface coverage and site blocking.

3.7.2.2. Potentiodynamic polarization (Tafel analysis). The potentiodynamic polarization curves in Fig. 10 demonstrate how MOME alters both anodic metal dissolution and cathodic hydrogen evolution kinetics.

The principal anodic and cathodic half-reactions for carbon steel in acidic media are expressed in Eq. (7) and (8):

$$Fe \longrightarrow Fe^{2+} + 2e^{-} \quad (7)$$

$$2H^{+} + 2e^{-} \longrightarrow H_2 \quad (8)$$

With increasing MOME concentration, the polarization curves shift to lower current densities for both branches, indicating effective suppression of both half-reactions. This behavior confirms the mixed-type inhibition previously inferred from OCP results. The inhibition efficiency IEp was calculated using Eq. (9):

$$IEp = \frac{i^{0}_{corr} - i_{corr}}{i^{0}_{corr}} \times 100 \quad (9)$$

According to Table 4, the corrosion current density decreases from 0.946 mA cm^{-2} for the blank solution to 0.11 mA cm^{-2} at 20 mg/L MOME, corresponding to an inhibition efficiency of 88.37%. Simultaneously, the polarization resistance Rp increases significantly, indicating the formation of a protective film that hinders charge-transfer reactions. Changes in the Tafel slopes, βa and βc, indicate that the inhibitor affects the kinetics of electron transfer by occupying reactive sites and altering the distribution of charge at the electrode surface. This effect is consistent with the adsorption of molecules containing heteroatoms such as oxygen and nitrogen and delocalized π-electrons, which are known to coordinate with transition metals and stabilize protective layers through both physical and weak chemical interactions [45,46].

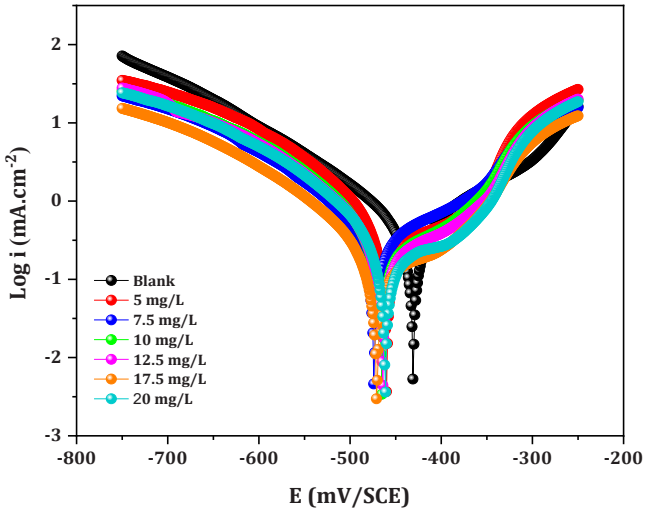

Fig. 10. Tafel polarization curves of X48 carbon steel in 1 M HCl at 25 °C, recorded without and with the addition of various concentrations of MOME inhibitor.

Table 4
Parameters were obtained through Tafel analysis at 25 °C in 1 M HCl, in the absence and presence of different MOME concentrations.

Cm (mg/L)	-E_{corr} (mV/ECS)	β_a (mV/dec)	-β_c (mV/dec)	R_p (Ω. cm^2)	i_{corr} (mA cm^{-2})	θ	IE_p (%)
Blank	497	179.4	138.2	50.96	0.946	-	-
5	460	164	100.7	55.56	0.47	0.5031	50.31
7.5	473	193.4	96.8	55.64	0.43	0.5454	54.54
10	463	135.2	106	71.72	0.385	0.5930	59.30
12.5	465	163	96.4	77.91	0.293	0.6902	69.02
17.5	470	136.6	86.4	89.88	0.141	0.8509	85.09
20	462	152	68.7	130.3	0.11	0.8837	88.37

The E_{corr} values obtained from polarization measurements are consistent with the OCP results presented in Fig. 9. Compared with the uninhibited solution (-497 mV/SCE), the inhibited systems exhibit slight positive shifts in corrosion potential, with E_{corr} values ranging from −460 to −473 mV/SCE. These relatively small displacements (<85 mV) indicate that MOME simultaneously affects both anodic and cathodic reactions, confirming its mixed-type inhibition behavior.

It should be noted that the open circuit potential (OCP) and the corrosion potential E_{corr} that come from polarization curves do not always match the surface states. OCP is taken when there is no disturbance, while E_{corr} is found using Tafel extrapolation during a forced scan. This scan can change the inhibitor film that is attached to the surface and change the cathodic reactions [45,46].

As shown in Fig. 10 and explained in Table 4, the OCP values move to positive potentials when the inhibitor is added. At the time, the E_{corr} values from the polarization curves move to potentials that are more negative. This pattern matches what happens when a film forms and when the Tafel slopes change.

The way the potential shifts in OCP and in the polarization data are different because the ways they are measured are different. This difference does not mean there is a problem with how the corrosion is being prevented.

3.7.2.3. Electrochemical impedance spectroscopy (EIS). Electrochemical impedance spectroscopy (EIS) is a highly informative technique for characterizing corrosion and inhibition processes. It provides quantitative insights into charge-transfer resistance, double-layer capacitance, and surface morphology at the metal–solution interface, revealing how inhibitor molecules modify electrochemical kinetics and interfacial structure. Nyquist plots obtained for carbon steel in 1 M HCl with and without MOME display single depressed semicircles (Fig. 11), whose centers lie below the real axis. This behavior reflects frequency dispersion due to surface heterogeneity, roughness, and adsorption effects rather than a purely kinetic process [47]. The absence of additional loops or secondary arcs confirms that corrosion is primarily governed by charge transfer, with negligible diffusional control. A progressive enlargement of the semicircle diameter with increasing MOME concentration indicates a marked increase in charge-transfer resistance (Rct), suggesting a slowdown in electron exchange between the metal and the electrolyte. This increase directly correlates with the growth of an adsorbed molecular layer that shields active sites and suppresses both anodic iron dissolution and cathodic hydrogen evolution.

Bode-phase plots (Fig. 12) further substantiate these findings. The progressive broadening and elevation of the phase angle maxima with inhibitor concentration indicate enhanced capacitive behavior and the formation of a continuous, compact, and insulating interfacial film [48,49]. At higher concentrations, the slope of log|Z| versus log f approaches −1, characteristic of an almost ideal capacitor. These spectral features suggest that MOME molecules reduce interfacial heterogeneity by replacing adsorbed water and chloride ions with organic components, thereby improving the surface dielectric uniformity.

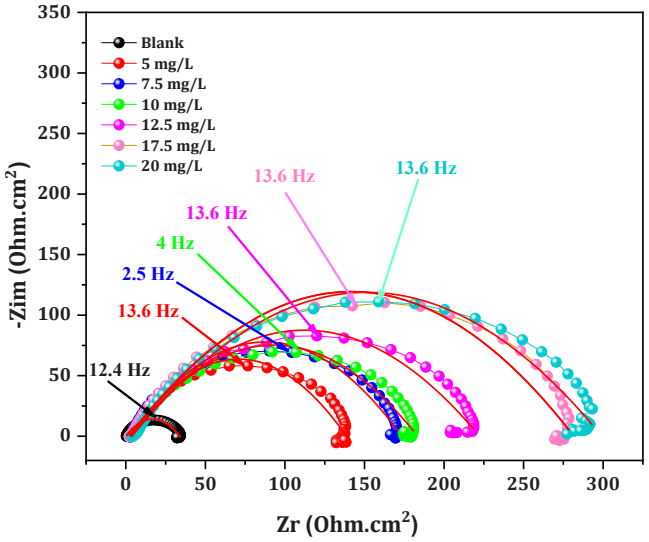

Fig. 11. Experimental (•) and fitted (–) Nyquist plots of carbon steel in 1 M HCl solution without and with different concentrations of MOME at 25 °C.

To quantitatively interpret the spectra, the impedance data were fitted using equivalent electrical circuits (EECs) shown in Fig. 13(c–d). Each circuit comprises a solution resistance (Rs) in series with a parallel combination of charge-transfer resistance (Rct) and a constant-phase element (CPEdl) representing the non-ideal double-layer capacitance. For inhibited systems, an additional Rf–CPEf branch accounts for the resistive and capacitive contributions of the protective film. Using constant phase elements instead of ideal capacitors ensures accurate modeling of systems affected by surface roughness, inhomogeneity, and frequency dispersion [50–53]. The effective interfacial capacitances (Cdl and Cf) were calculated from the fitted parameters using the following relation (Brug et al.):

$$C = \left[Q(R_s^{-1} + R_{ct}^{-1})^{n-1}\right]^{1/n} \quad (10)$$

where C is the equivalent capacitance (F·cm^{-2}), Q is the CPE constant ($\Omega^{-1}\cdot s^n\cdot cm^{-2}$), R is the corresponding resistance (Rct and Rs), and n is the CPE exponent ($0 \leq n \leq 1$) describing the deviation from ideal capacitive behavior. As n→1, the CPE approaches an ideal capacitor, indicating a smooth and homogeneous interface. The fitted data exhibited very low χ^2 values (10^{-3}–10^{-4}), confirming the robustness of the model.

A comparison of the impedance parameters with literature data reveals electrochemical signatures similar to those reported for organic inhibitors that form compact adsorbed films, namely, an increase in Rct accompanied by a decrease in Cdl [54,55]. This parallel behavior confirms that MOME induces a surface-stabilization mechanism comparable to that of MOME, dominated by charge-transfer suppression through molecular adsorption.

The inhibition efficiency was calculated from the charge-transfer resistance (Rct), which is directly associated with the corrosion kinetics at the metal/solution interface, according to Eq. (11):

$$IE_{EIS} = \frac{\mathrm{Rct(inh)} - \mathrm{Rct}^{\circ}}{\mathrm{Rct(inh)}} \times 100 \quad (11)$$

where Rct(inh) and Rct° are the charge-transfer resistances in the absence and presence of the inhibitor, respectively.

As shown in Table 5, Rct increased dramatically from 34.43 Ω·cm^2 for the blank solution to 270.5 Ω·cm^2 at 20 mg·L^{-1} MOME, while Rf increased from zero to 69.59 Ω·cm^2. Consequently, the overall polarization resistance (Rp = Rf + Rct) increased substantially, confirming that MOME strongly impedes the corrosion process at the steel–solution interface. In parallel, the recalculated double-layer capacitance (Cdl) values decreased markedly with increasing inhibitor concentration, indicating progressive adsorption of MOME constituents on the steel surface. This decrease may be attributed to: (i) the displacement of adsorbed water molecules and chloride ions by inhibitor molecules, (ii) a reduction in the local dielectric constant at the interface, and (iii) an increase in the thickness of the adsorbed protective layer. The continuous increase in both Rct and Rf demonstrates the formation of an increasingly effective barrier against charge transfer and ionic transport.

The relatively lower capacitance values obtained in the presence of MOME support the formation of a compact organic layer covering the steel surface. Furthermore, the CPE exponent n_2 decreased from 0.8757 for the blank solution to 0.7591 at 20 mg·L^{-1} MOME, indicating a greater deviation from ideal capacitive behavior and an increase in interfacial heterogeneity. Such behavior is commonly observed in systems containing adsorbed organic layers, where non-uniform surface coverage, variations in adsorption strength, and the multicomponent nature of plant extracts contribute to a broader distribution of relaxation times at the metal/electrolyte interface. Therefore, the decrease in n_2 should not be interpreted as evidence of surface smoothing. Instead, conclusions regarding surface morphology are supported by AFM and optical microscopy analyses. Such behavior is commonly observed for adsorption

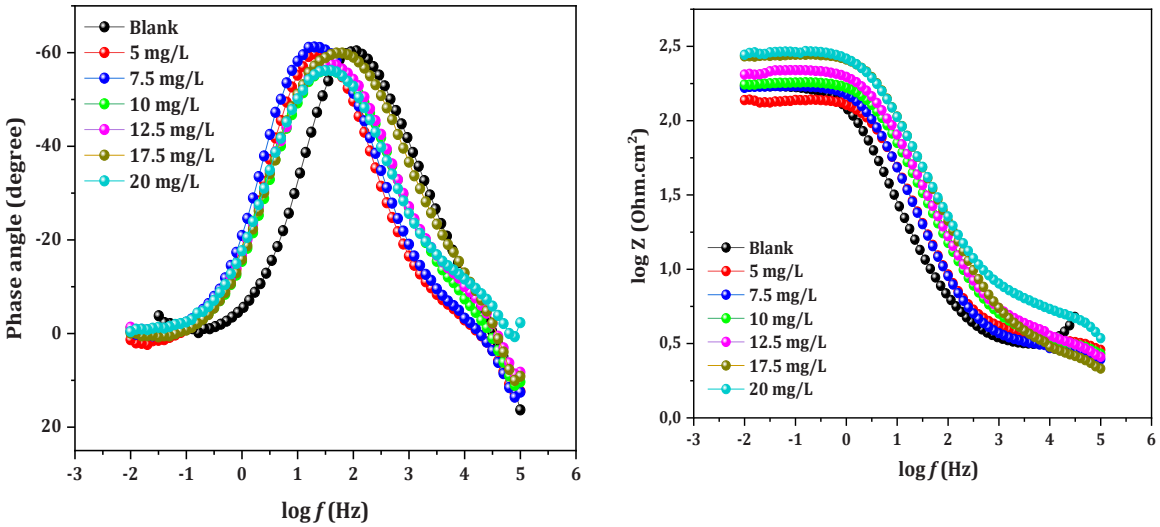

Fig. 12. Phase angle and Bode plots illustrating the effect of methanolic extract MOME concentrations in HCl 1 M at 25 °C.

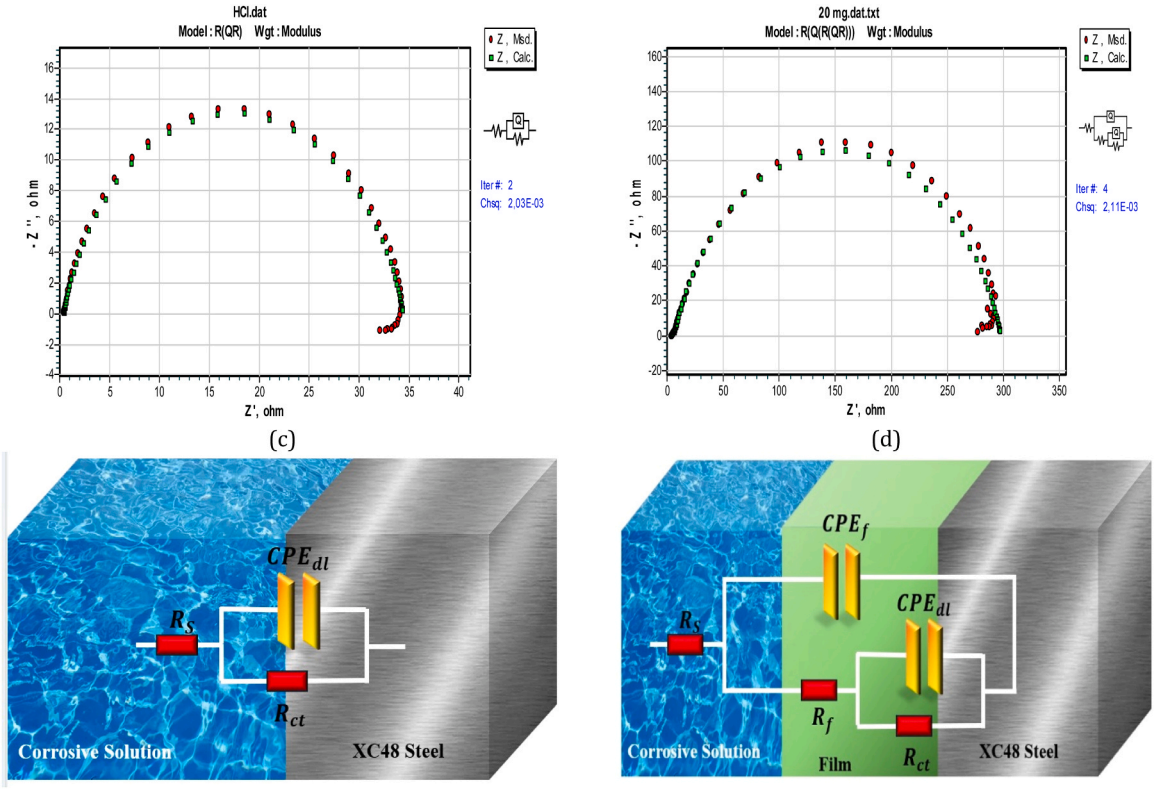

Fig. 13. Nyquist plots (measured with ZsimpWin) of mild steel in 1 M solution of HCl: (red) experimental data; (green) fitted data. (a) uninhibited solution; (b) 20 mg/L of MOME extract; (c) equivalent circuit of the uninhibited solution; (d) equivalent circuit of the inhibited solution. Measurements of the corrosion of carbon steel in 1.0 M HCl in the absence and presence of various concentrations of MOME extract at 25°C.

Table 5
Impedance parameters of carbon steel in HCl 1 M at different concentrations of methanolic extract **MOME** at 25 °C.

Inhibitor	*Cm (mg/ L)*	*Rs (Ω. cm^2)*	*R_f (Ω. cm^2)*	*CPE_f*		*C_f ($\mu F/ cm^2$)*	*Rct (Ω. cm^2)*	*CPE_{dl}*		*C_{dl} ($\mu F/ cm^2$)*	*$\chi^2 \times 10^{-3}$*	*R_p (R_f+R_{ct})*	*θ*	IEEIS (%)
				Q1 ($\mu\Omega^{-1}s^n cm^{-2}$)	*n1*			*Q2 ($\mu\Omega^{-1}s^n cm^{-2}$)*	*n2*					
Blank	0	0.4198	-	-	-	-	34.43	474.9	0.8757	141.4	2.03	34.43	-	-
MOME	5	3.453	2.885	205.3	0.8	32.03	131.2	447.2	0.8475	138.8	4.43	134.08	0.7432	73.75
	7.5	2.885	3.297	141	0.7891	18.13	166.7	350	0.844	97.49	4.54	169.99	0.7974	79.34
	10	3.285	6.607	65.36	0.7744	6.84	181.2	336.9	0.841	92.72	6.29	187.80	0.8166	80.99
	12.5	3.373	11.06	64.1	0.7541	6.02	198.4	206.9	0.8184	41.09	3.71	209.46	0.8356	82.64
	17.5	2.565	23.99	7.073	0.5817	1.38×10^{-2}	231.3	155.5	0.7654	14.07	4.63	255.29	0.8651	85.11
	20	4.837	69.59	4.763	0.5162	2.61×10^{-3}	270.5	135.2	0.7591	13.12	2.11	340.09	0.8987	87.27

layers formed from multicomponent plant extracts. Overall, the EIS results strongly support an adsorption-controlled inhibition mechanism. The significant increase in Rct and Rf, together with the decrease in Cdl, suggests that the phytochemical constituents of MOME adsorb onto the steel surface through a combination of electrostatic interactions and donor–acceptor interactions involving oxygen-containing functional groups and π-electron systems. Similar impedance responses have been reported for other plant-derived corrosion inhibitors, confirming the formation of a protective organic film that effectively suppresses metal dissolution in acidic media [56–59].

In summary, MOME exhibits mixed-type corrosion-inhibition behavior, achieving nearly 90% inhibition efficiency at 20 mg·L^{-1} . The EIS results conclusively show that the inhibitor molecules adsorb strongly onto the steel surface, forming a compact dielectric film that suppresses both anodic and cathodic reactions. These findings align closely with polarization and gravimetric analyses, confirming that MOME acts as an efficient, sustainable, and environmentally friendly inhibitor for carbon steel in acidic media.

3.7.2.4. Interpretation of impedance parameters. The impedance parameters listed in Table 5 exhibit a coherent, systematic evolution with inhibitor concentration. The steady increase in Rct and Rf, together with the pronounced decline in Cdl and Cf, confirms that MOME molecules progressively build an adherent, insulating film that limits both electron transfer and ionic diffusion across the metal–solution interface. The continuous growth in Rp indicates cumulative film reinforcement, whereas the near-linear correlation between θ and concentration suggests Langmuir-type adsorption behavior. The consistency between the Nyquist and Bode representations was carefully verified. For the uninhibited solution, the low-frequency impedance response agrees well with the charge-transfer resistance obtained from equivalent-circuit fitting (Rct = 34.43 Ω·cm^2). This value is consistent with the low-frequency intercept observed in the Nyquist diagram and confirms that charge-transfer mechanisms predominantly govern the corrosion process. The presence of a single depressed capacitive loop and a single relaxation process in the Bode phase plot further supports this interpretation. The reduction of Cdl from 474.9 to 135.2 μF·cm^{-2} and Cf from 205.3 to 4.76 μF·cm^{-2} reflects the displacement of hydrated ions and

water molecules by adsorbed organic species with lower dielectric constants, producing a dense organic barrier with higher resistivity. Simultaneously, the gradual decrease in n_1 and n_2 values indicates that the interfacial layer becomes increasingly homogeneous and less porous. These results, coupled with the low χ^2 fitting errors (2.11×10^{-3} to 6.29×10^{-3}) and the close overlap between the experimental and fitted spectra, indicate excellent fitting quality and confirm the formation of a stable, well-organized protective layer.

Overall, the impedance analysis demonstrates that MOME adsorption results in the formation of a continuous, low-permittivity, corrosion-resistant film. The high polarization resistance (340.09 Ω·cm²) and inhibition efficiency (87.27%) at 20 mg·L^{-1} confirm that the adsorbed molecules effectively block charge-transfer pathways and stabilize the steel surface against acid-induced dissolution.

3.7.3. Adsorption isotherm

The inhibition of metal corrosion by organic compounds is generally explained by adsorption. Adsorption can occur via two principal mechanisms: physical and chemical. The prevailing mechanism depends on several factors, including the charge and nature of the metal surface, the organic compound's chemical characteristics, and the electrolyte's composition.

In the present study, different adsorption isotherm models were employed to identify the most appropriate description of the adsorption process, specifically the Langmuir, Temkin, and Frumkin isotherms. Figs. 14a, 14 b, and 14c illustrate the fitting of the experimental data to these models. According to these isotherms, the surface coverage (θ) is related to the inhibitor concentration (C_{inh}) through the corresponding Eqs. (12, 13, and 14) [59,60]. The Temkin isotherm assumes that the adsorption energy decreases linearly with increasing surface coverage, thereby accounting for interactions between the adsorbed molecules. This feature distinguishes it from the Langmuir isotherm, which assumes uniform adsorption sites and no interactions among adsorbates, and the Frumkin isotherm, which introduces a parameter to quantify lateral interactions between adsorbed species.

$$\exp(-2\alpha\theta) = K_{ads}C_{inh} \tag{12}$$

In this context, K_{ads} represents the adsorption equilibrium constant, while α indicates the interaction parameter among the adsorbed molecules. The Frumkin isotherm accounts for lateral interactions among adsorbed particles, incorporating the potential for either repulsive or attractive forces, as represented by the following expression:

$$\left(\frac{\theta}{1-\theta}\right)\exp(-2\alpha\theta) = \quad K_{ads}C_{inh} \tag{13}$$

In contrast, the Langmuir isotherm assumes that the adsorption sites are uniform and that each site accommodates only a single molecule, described by the following relation:

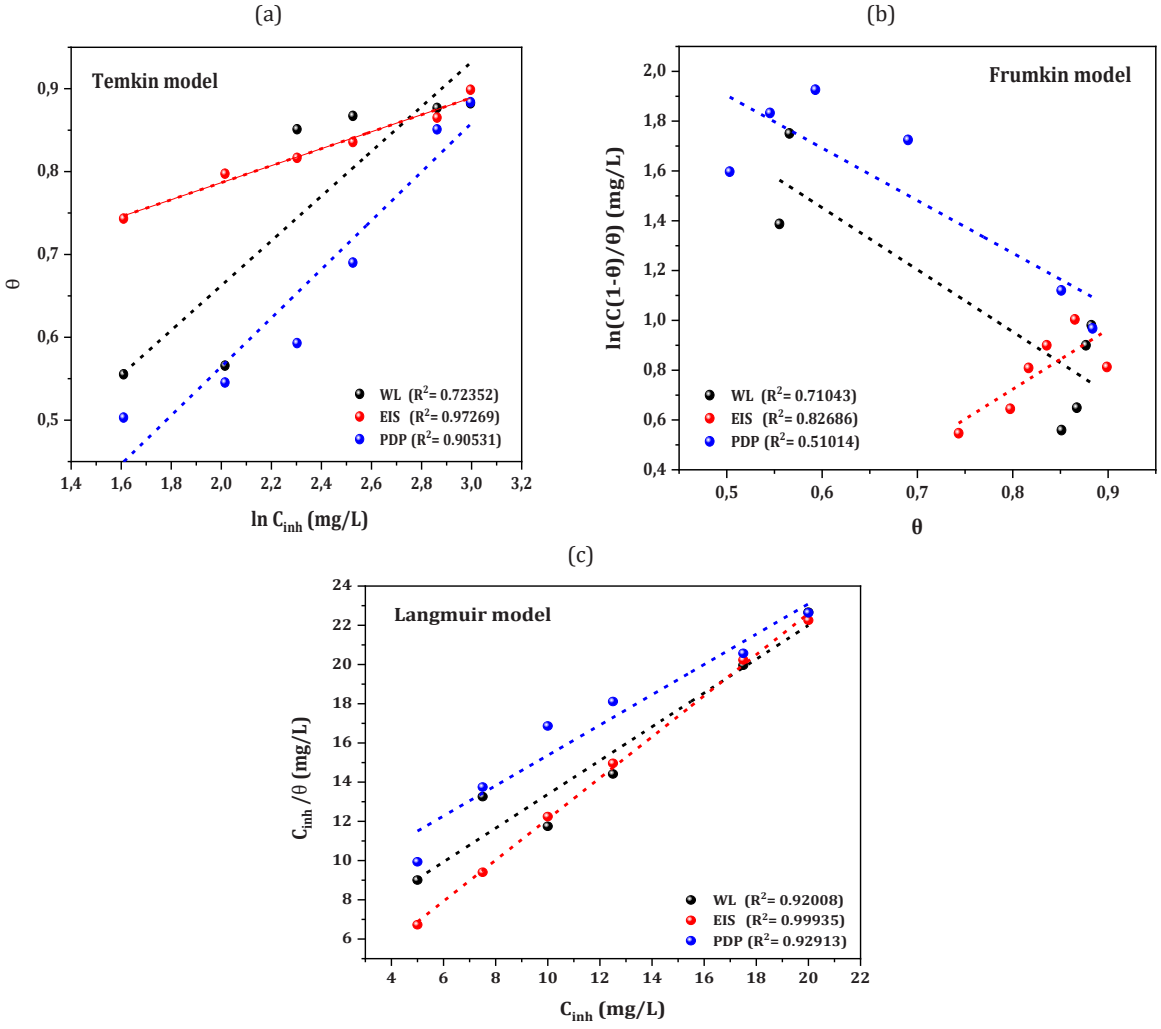

Fig. 14. Adsorption isotherm plots (a) Temkin, (b) Frumkin, (c) Langmuir for X48 carbon steel in 1 M HCl in the presence of methanolic extract MOME inhibitor for the three methods at 25 ∘C.

$$\frac{C_{inh}}{\theta} = \frac{1}{K_{ads}} + C_{inh} \quad (14)$$

The most suitable adsorption isotherm was determined from data obtained using three techniques, namely potentiodynamic polarization (PDP), weight loss (WL), and electrochemical impedance spectroscopy (EIS). As shown in Fig. 14 and summarized in Tables 3–5, the adsorption data obtained from weight-loss, PDP, and EIS measurements were analyzed using different adsorption models. Among the tested models, the Langmuir isotherm provided the most consistent overall description of the experimental results, with correlation coefficients of $R^2 = 0.92008$, 0.99935, and 0.92913 for the WL, PDP, and EIS data, respectively.

Although alternative models, such as the Temkin model, also provided reasonable fits for some datasets, the Langmuir model was retained because it yielded the most consistent adsorption parameters across the different experimental techniques. The applicability of the Langmuir model suggests that adsorption occurs predominantly through the formation of an adsorbed inhibitor layer on the steel surface. However, given the complex multicomponent nature of MOME, the assumptions of perfectly homogeneous adsorption sites and complete absence of adsorbate–adsorbate interactions should be regarded as an idealized approximation rather than a strict physical description of the system. Therefore, the Langmuir model is used here primarily as a useful mathematical framework for describing the adsorption behavior and estimating the associated thermodynamic parameters. The good agreement between the experimental data and the Langmuir model supports the formation of a protective adsorbed layer resulting from interactions between the phytochemical constituents of MOME and the carbon steel surface [61,62]. The thermodynamic feasibility and spontaneity of the adsorption process were further evaluated by calculating the standard Gibbs free energy of adsorption (ΔG°ads), using the following expression:

$$\Delta G^0_{ads} = -RT\ln\left(10^6 \times K_{ads}\right) \quad (15)$$

where R is the universal gas constant, T is the absolute temperature (K), and 10^6 mg L^{-1} represents the concentration of water expressed in units consistent with the inhibitor concentration.

A limitation of the present study is the absence of temperature-dependent corrosion measurements. Such experiments would allow the determination of the activation energy (Ea), activation enthalpy (ΔHa), and activation entropy (ΔSa), providing additional insight into the adsorption mechanism and the relative contributions of physical and chemical interactions. Although the apparent ΔG°ads values (approximately −34 kJ mol^{-1}) suggest a mixed adsorption mechanism [3], a more rigorous thermodynamic assessment would require corrosion measurements at different temperatures. This aspect will be considered in future work. where R is the universal gas constant, T is the absolute temperature (K), and 10^6 mg L^{-1} represents the concentration of water expressed in units consistent with the inhibitor concentration. Because MOME is a multicomponent plant extract, no unique molecular weight can be assigned to the inhibitor system. Consequently, the calculated Kads and ΔG°ads values should be regarded as apparent thermodynamic parameters describing the overall adsorption behavior of the extract rather than that of a single molecular species. Analysis of the Langmuir adsorption model yielded a negative apparent standard Gibbs free energy of adsorption (ΔG°ads), indicating that adsorption of MOME constituents onto the carbon steel surface is spontaneous (Table 6). The calculated apparent ΔG°ads values (approximately −34 kJ mol^{-1}) suggest a mixed adsorption mechanism involving both physical and chemical contributions [3]. Such behavior may arise from electrostatic interactions between protonated phytochemical species and the charged metal surface, as well as donor-acceptor interactions involving oxygen-containing functional groups and π-electron systems present in the polyphenolic constituents of the extract.

Table 6
Thermodynamic parameters for the adsorption of methanolic extract MOME for inhibiting corrosion in carbon steel by 1 M HCl at a temperature of 25°C.

Methods	R^2	K_{ads} (mg/L)$^{-1}$	$-\Delta G_{ads}$ (kJ mol^{-1})
WL	0.92008	1.16037	34.4
ESI	0.99935	0.94861	33.9
PDP	0.92913	1.29441	34.7

3.7.4. UV–visible analysis

Vegetable-derived corrosion inhibitors have attracted significant research interest due to their ability to form protective complexes on metal surfaces. Compounds of particular relevance are those capable of chelating metal ions, forming insoluble surface complexes that suppress corrosion. UV–visible spectroscopy was performed to examine the potential formation of MOME–Fe complexes via coordination with iron ions released during corrosion. Fig. 15 presents the comparative absorption spectra of inhibitor solutions (20 mg/L) in their initial state (black curve, before steel immersion) and after 4 days of carbon steel exposure (red curve).

The UV-Vis spectrum of MOME before steel immersion exhibited a distinct absorption band at λmax = 218 nm, which can be attributed to π→π* transitions associated with aromatic rings and conjugated unsaturated systems present in the phytochemical constituents of the extract [50]. After four days of immersion, significant spectral changes were observed. A new absorption band appeared around 350 nm, which may be assigned to π→π* transitions within extended conjugated systems and/or to changes in the electronic environment of the phenolic constituents following interaction with iron species. In addition, a shoulder at approximately 236 nm was observed, which may be related to electronic transitions involving heteroatom-containing functional groups. A broad absorption feature was also detected near 888 nm. Since n→π* transitions of oxygen-containing functional groups generally occur in the UV region, this near-infrared band cannot be attributed to such transitions. Instead, it is more plausibly associated with ligand-to-metal charge transfer (LMCT) processes and/or d–d electronic transitions arising from interactions between dissolved iron species and the polyphenolic constituents of the extract. Similar spectral features have been reported for iron-polyphenol coordination systems, in which hydroxyl and carboxyl groups act as electron donors. Overall, the spectral modifications observed after immersion suggest interactions between iron species and the phytochemical constituents of MOME. These interactions are consistent with the formation of a protective adsorbed

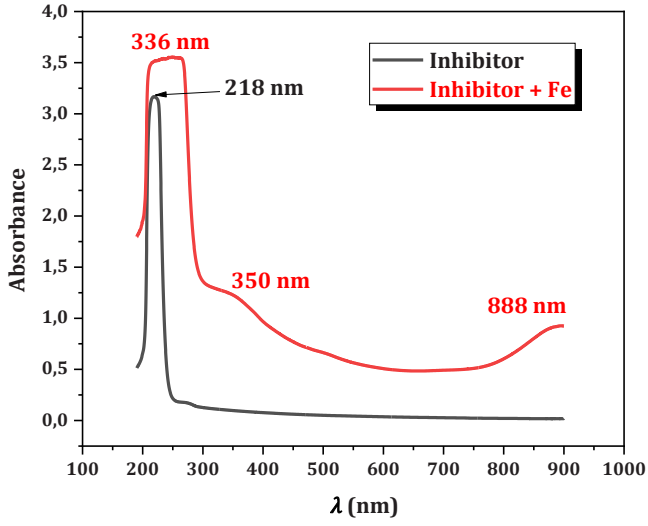

Fig. 15. The recorded UV/Vis spectra before and after immersion of carbon steel.

layer and may contribute to the inhibition of corrosion. However, the UV-Vis results should be regarded as supportive evidence of inhibitor–metal interactions rather than definitive proof of a specific adsorption mechanism.

3.7.5. Surface examination

3.7.5.1. AFM method. Atomic Force Microscopy (AFM) was used to investigate the surface morphology of carbon steel using 2D and 3D mapping. Comparative micrographs are shown in Fig. 16 for (a) abraded pristine mild steel, (b) steel immersed in 1 M HCl solution, and (c) steel immersed in 1 M HCl containing the optimum concentration of MOME extract (20 mg/L).

To complement the qualitative AFM observations, the average roughness (Ra) and root-mean-square roughness (RMS) were determined and summarized in Table 7. The uninhibited surface exhibited substantially higher roughness values due to severe acid attack. In contrast, the inhibited surface showed significantly lower Ra and Rq values, indicating the formation of a protective adsorbed layer that mitigates surface degradation. The polished carbon steel surface exhibited very low roughness values Ra = 13.387 nm and RMS = 17.765 nm), indicating a smooth, homogeneous substrate. After immersion in 1 M HCl, the roughness increased markedly toRa = 428.869 nm and RMS = 532.237 nm, reflecting severe surface deterioration resulting from corrosive attack.

In the presence of 20 mg/L MOME, the roughness values decreased toRa = 339.131 nm and RMS = 455.440 nm. This reduction in surface roughness indicates that the inhibitor mitigated acid-induced damage by adsorbing onto the steel surface and forming a protective film that partially limited the development of corrosion defects. Although the inhibited surface remained rougher than the polished substrate, the AFM results clearly demonstrate improved surface integrity compared with the uninhibited specimen. These observations are consistent with the electrochemical, gravimetric, and surface characterization results, further confirming MOME's corrosion-inhibition performance.

3.7.5.2. Optical microscopy. The electrode surfaces were examined macroscopically after 24 h of immersion in an aggressive 1 M HCl solution, both in the absence and presence of the MOME inhibitor at its optimum concentration of 20 mg/L (Fig. 16). In the uninhibited medium, the steel surface exhibited severe corrosion damage (Fig. 16-b) compared to its initially polished condition (Fig. 16-a). In contrast, the surface showed markedly reduced degradation in the inhibited solution, forming a relatively uniform protective film (Fig. 16-c). This observation highlights MOME's efficiency in mitigating corrosion and enhancing surface protection, even under quiescent conditions (Fig. 17).

Table 7
AFM roughness parameters of carbon steel surfaces.

	Polished carbon steel	Carbon steel + 1 M HCl	Carbon steel + 1 M HCl + 20 mg/L MOME
RMS (nm)	17.765	532.237	455.440
Ra (nm)	13.387	428.869	339.131

3.8. Comparison with available literature

Natural plant extracts have attracted significant attention as environmentally friendly corrosion inhibitors because of their renewability, abundance of bioactive compounds, and relatively low toxicity. In this context, the methanolic extract of *Moringa oleifera* fruits (MOME) was compared with other reported plant-based inhibitors. As summarized in Table 8, MOME achieved 89.87% inhibition efficiency at 20 mg/L in 1 M HCl.

It should be noted that the inhibitors listed in Table 7 were evaluated under different experimental conditions, including variations in steel grade, corrosive medium, inhibitor concentration, immersion time, and temperature. Consequently, direct quantitative comparison of inhibition efficiencies should be interpreted with caution. The table is primarily intended to provide a general perspective on the performance of plant-derived corrosion inhibitors reported in the literature, rather than to establish a rigorous ranking of inhibitor effectiveness. This performance is comparable to that of several plant extracts reported in the literature, while requiring a lower dosage than many of them. For example, betel leaf extract reached 94.90% inhibition at 400 mg/L [63], Ficus tikoua leaf extract reached 93.80% at 200 mg/L [64], Laurus nobilis extract reached 92.00% at 400 ppm [65], and Elaeoselinum thapsioides reached 82.00% at 900 mg/L [66]. Although some extracts, such as *Thymus vulgaris* and *Fraxinus excelsior,* achieved similar or slightly higher efficiencies at comparable concentrations [46,67], the results obtained with MOME still demonstrate strong protection at relatively low dosage. The inhibition effect may be attributed to the phenolic and flavonoid constituents of the extract, which possess oxygen-containing functional groups and aromatic π-electron systems that favor interaction with the steel surface. These interactions likely contribute to the formation of an adsorbed protective layer, as suggested by the electrochemical, adsorption, and surface characterization results. Although the extract also displayed antioxidant activity, its antimicrobial effect was limited under the tested conditions. Therefore, the principal value of MOME lies in its corrosion-inhibition performance rather than in broad multifunctional bioactivity. Overall, this comparison highlights the potential of MOME as a natural, low-dose inhibitor for sustainable corrosion protection.

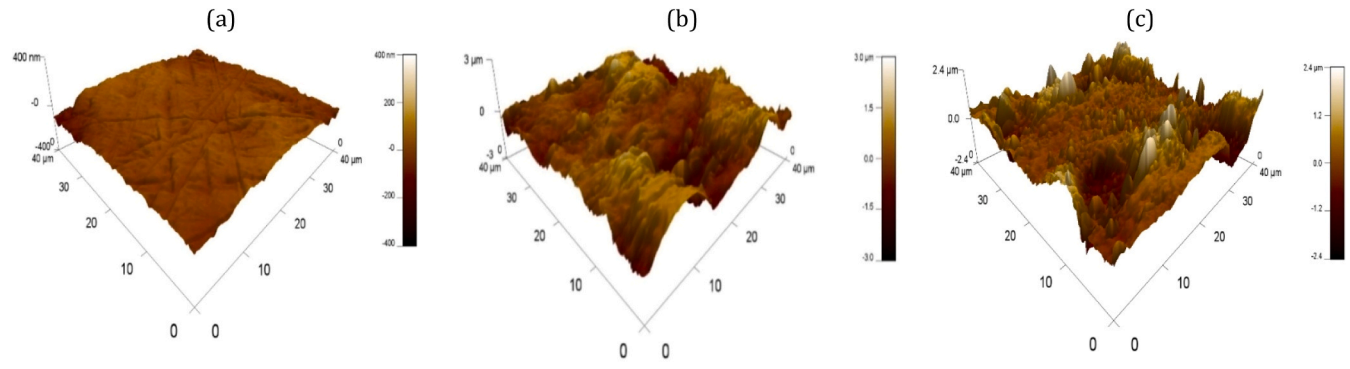

Fig. 16. Three-dimensional AFM images of the MOME extract surface in 1 M HCl solution after 24 h of immersion (a) Polished surface; (b) without inhibitor; (c) with 20 mg/L of the MOME extract inhibitor.

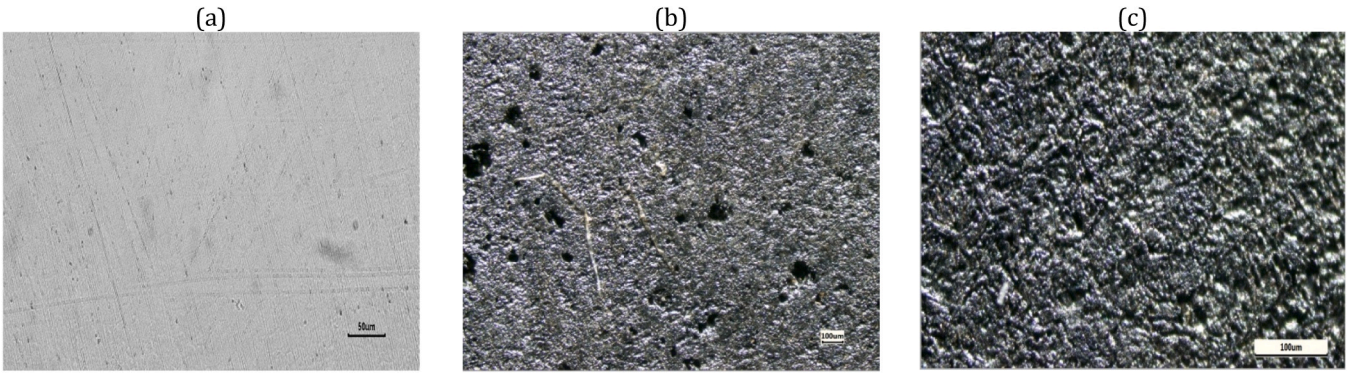

Fig. 17. Photographic images of the MOME extract surface in 1 M HCl solution after 24 h of immersion: (a) polished surface, (b) without inhibitor, and (c) with 20 mg/L of the MOME extract.

Table 8
Comparison of the inhibition efficiencies of the MOME with other inhibitors from the literature.

Inhibitor structure	Medium	Substrate	Concentration	Efficiency	Reference
Thymus vulgaris L.	1 M HCl	Carbon steel X48	12.5 mg/L		[46]
Butanol extract				92.23%	
Chloroform extract				90.55%	
Betel L.	1 M HCl	Carbon steel X48	400 mg/L	94.90%	[63]
Ficus tikoua leaves	1 M HCl	Carbon steel	200 mg/L	93.80%	[64]
Laurus nobilis L	1 M HCl	Carbon steel	400 ppm	92.00%	[65]
Fraxinus excelsior	1 M HCl	Carbon steel X48	12.5 mg/L	89.58%	[66]
Elaeoselinum thapsioides L.	1 M HCl	Carbon steel	900 mg/L	82.00%	[67]
Taxus baccata L.	1 M HCl	Carbon steel			[53]
Methylene dichloride extract			600 ppm	79.04%	
Ethyl acetate extract			800 ppm	82.08%	
n-Butanol extract			700 ppm	74.26%	
Glebionis Coronaria L.	1 M HCl	Carbon steel	10^{-3} M	79.00%	[68]
MOME	1 M HCl	Carbon steel X48	20 mg/L	89.87%	This work

3.9. Molecular docking

The molecular docking results revealed favorable binding affinities between several identified phytochemicals and the selected biological targets. Among the investigated compounds, rutin, quercetin, and ellagic acid exhibited the strongest interactions with the antioxidant-related enzymes. It should be noted that the molecular docking approach was not employed to model the adsorption of phytochemical compounds onto the carbon steel surface. The corrosion inhibition mechanism was established through electrochemical measurements, adsorption studies, surface analyses, and quantum-chemical calculations. Therefore, the docking results should be interpreted exclusively as supporting evidence for the antioxidant properties of the identified phytochemicals, which may indirectly contribute to corrosion protection by limiting oxidative processes and enhancing the stability of the protective adsorbed film.

The docking results presented in Table 9, together with the interaction diagrams compiled in Fig. 18 (a–h), allow a comparative interpretation of how the phenolic and flavonoid compounds identified by HPLC interact with the enzymes catalase (PDB 2CAG), glutathione peroxidase (PDB 2P31), superoxide dismutase (PDB 1CB4), and the corrosion-associated enzyme of Acidithiobacillus ferrooxidans (1HIO).

The binding free energy (ΔG) and the inhibition constant (Ki) reflect the thermodynamic tendency of each compound to bind the enzyme's active or regulatory regions. A lower Ki indicates a higher binding affinity, meaning a lower inhibitor concentration is required to reduce enzyme activity significantly. This relationship is expressed mathematically by Eq. (16), which relates the free energy of binding to inhibitory strength [69,70]:

$$K_i = \exp(\Delta G/RT) \tag{16}$$

where ΔG is the binding free energy (kcal mol^{-1}), R is the universal gas constant (1.987 × 10^{-3} kcal mol^{-1} K^{-1}), and T is the temperature (298 K). A more negative ΔG corresponds to a lower Ki, reflecting stronger inhibitor binding. However, it must be noted that docking estimates represent static interactions in a rigid binding site and do not directly measure catalytic displacement, solvent effects, or conformational adaptation. Therefore, these values indicate mechanistic plausibility rather than confirmed biological inhibition.

Across all targets, a clear ranking emerges: rutin shows the highest affinity, followed by ellagic acid, then quercetin, and finally chlorogenic acid. This order aligns with structural considerations. Rutin and ellagic acid have extensive hydroxylation and extended aromatic conjugation, allowing multiple hydrogen bonds and π interactions. In contrast, chlorogenic acid exhibits comparatively limited conformational adaptability within the binding pockets. In Fig. 18 (a), rutin binds catalase with ΔG approximately minus 11 kcal mol^{-1} and Ki approximately 0.01 μM. It establishes multiple hydrogen bonds with Phe 313, Arg 333, and Tyr 337, as well as π- π stacking with Phe 140, forming a tightly interlocked network that suggests a competitive-type inhibition mode by occupying or sterically shielding the catalytic cavity. In Fig. 18 (b), ellagic acid displays ΔG approximately minus 10.1 kcal mol^{-1} and Ki approximately 0.04 μM, forming directional hydrogen bonding with Phe 313, Arg 344, His 54, and Ala 312, along with a π cation interaction with Arg 51. Compared with rutin, the stabilizing forces differ in balance, suggesting that both could inhibit catalase but potentially through slightly different geometric anchoring modes.

In Fig. 18 (c), rutin interacts with glutathione peroxidase mainly through nonpolar and π-type contacts involving Ala 66 and Val 165, accompanied by two hydrogen bonds with Arg 65 and Arg 169. The stabilization here appears to rely more on hydrophobic packing rather than extensive directional bond networks. This difference implies that inhibition of glutathione peroxidase may be more sensitive to temperature, solvent, and conformational mobility than catalase inhibition. Fig. 18 (d), (e), and (f) illustrate ligand binding with superoxide

Table 9
Score results of interactions between enzyme receptors and ligands.

Molecules	Catalase (2CAG)		Glutathione Peroxidase (2P31)		SOD (1CB4)		Acidithiobacillus ferrooxidans (1HIO)	
	Energy (kcal/mol)	Ki (μM)	Energy (kcal/mol)	Ki (μM)	Energy (kcal/mol)	Ki (μM)	Energy (kcal/mol)	Ki (μM)
Caffeic acid	-7.1	6.25	-4.9	256.02	-5.6	78.55	-7.2	5.28
Chlorogenic acid	-8.8	0.35	-6.7	12.27	-8	1.37	-8.8	0.35
Cinnamic acid	-7	7.40	-4.8	303.09	-6.2	28.53	-7.1	6.25
Coumaric acid	-7.6	2.69	-5.1	182.67	-6.1	33.78	-7.7	2.27
Ellagic acid	-10.1	0.04	-6.8	10.36	-8	1.37	-8.5	0.59
Ferulic acid	-7.4	3.76	-4.7	358.82	-5.6	78.55	-7.3	4.46
Gallic acid	-8.8	0.35	-6.8	10.36	-7.8	1.92	-8.9	0.30
Hesperentin	-9.3	0.15	-6.2	28.53	-7.3	4.46	-9.2	0.18
Quercetin	-9.6	0.09	-6.8	10.36	-8	1.37	-9.7	0.08
Rosmarinic	-9.8	0.07	-6.9	8.76	-6.9	8.76	-7.8	1.92
Rutin	-11	0.01	-8	1.37	-7.5	3.18	-10.6	0.02
Syringic acid	-6.1	33.78	-4.6	424.79	-6.1	33.78	-6.7	12.27
Vanillin	-6.4	20.36	-4.5	502.89	-5	216.26	-6.3	24.10
Ascorbic acid	-6	39.99	-5.5	93.00	-5.6	78.55		

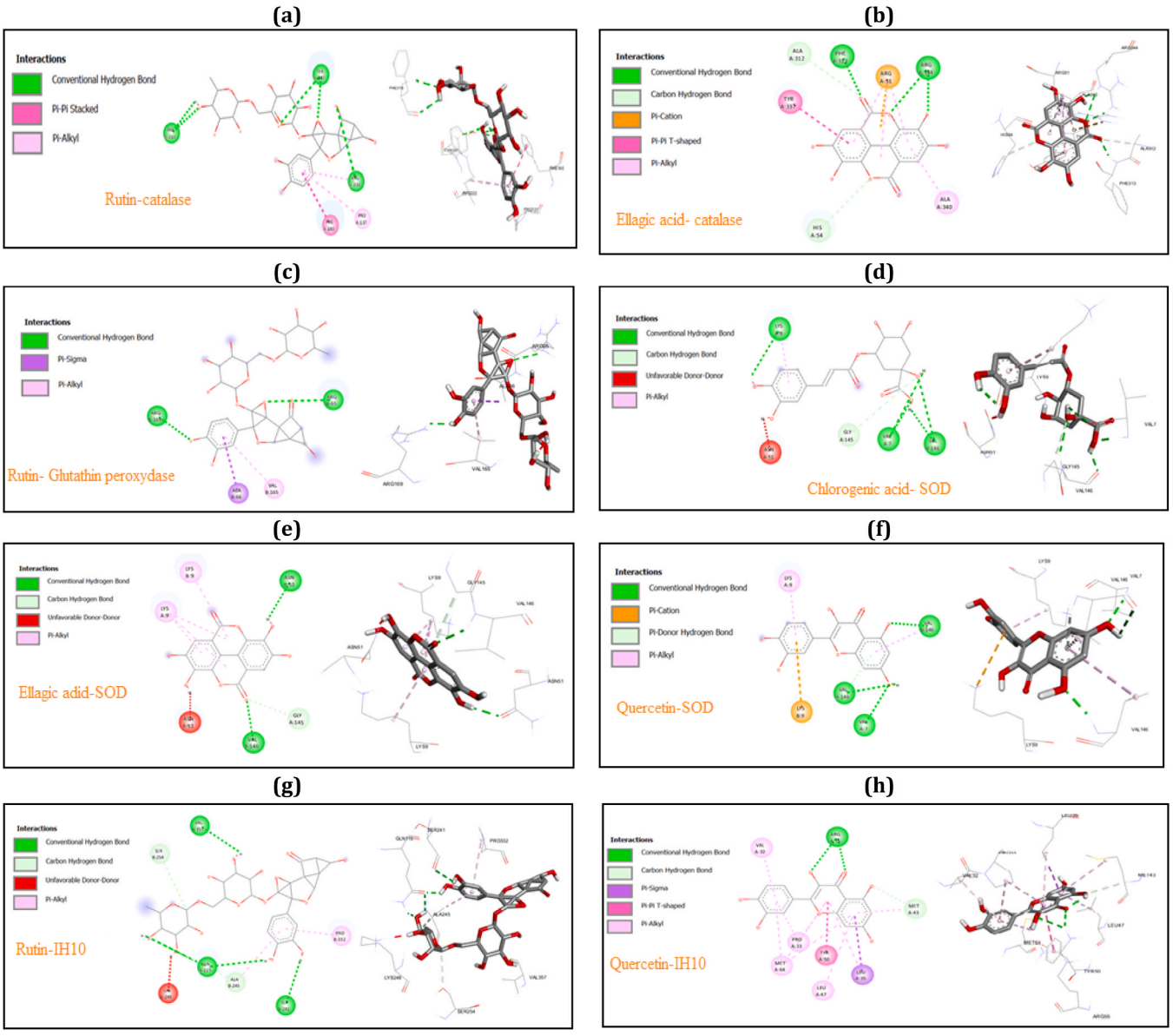

Fig. 18. 2D and 3D receptor-ligand interaction diagrams.

dismutase. Chlorogenic acid forms several hydrogen bonds with Val 146 and Ala 7 but produces fewer secondary contacts, explaining its higher

Ki (approximately 1.37 μM). Ellagic acid and quercetin, on the other hand, form richer π-alkyl and π cation interactions with Lys 9. These residues are located near regions involved in redox electron transfer, suggesting that inhibition may arise not from direct obstruction of the active site but from disturbance of local electrostatic fields necessary for catalytic cycling. This introduces a distinct mechanistic interpretation: the inhibition may be noncompetitive or mixed-mode, affecting the electron relay rather than substrate accessibility.

In Fig. 18 (g) and (h), rutin and quercetin bind to the Acidithiobacillus ferrooxidans 1HIO enzyme with high affinity. Rutin forms multiple conventional hydrogen bonds, carbon-hydrogen interactions, and π-alkyl contacts, corresponding to Ki approximately 0.02 μM, indicating stable binding. Quercetin displays a slightly higher Ki (approximately 0.08 μM), but stabilization is achieved through numerous hydrophobic and π interactions. These results imply that rutin may act not only as an antioxidant inhibitor of radical-scavenging enzymes but also interfere with microbial iron metabolism and electron-transfer processes linked to biocorrosion. However, this interpretation assumes that the enzyme is accessible within the microbial matrix and that in vitro binding translates to functional suppression under biological conditions. Such assumptions require biochemical and microbiological verification, since docking cannot evaluate enzyme accessibility in biofilm systems or conformational plasticity during catalysis.

Taken together, the docking analysis supports the conclusion that structurally complex and highly substituted flavonoids, such as rutin, exhibit the greatest inhibitory potential across multiple enzyme targets, followed by ellagic acid and quercetin. In contrast, smaller phenolic acids, such as chlorogenic acid, display weaker but still meaningful binding capacity. The pattern follows a logical structure-function relationship in which the number and spatial arrangement of hydroxyl groups, the extent of aromatic surface exposure, and conformational adaptability determine the richness and stability of ligand-protein interactions. However, the interpretation of inhibitory potency remains predictive rather than confirmatory and will require kinetic assays, catalytic turnover measurements, or molecular dynamics simulations to be fully validated. Thus, while Table 8 and Fig. 18 (a–h) demonstrate a clear thermodynamic preference for binding, the translation into biological inhibition remains an open, experimentally testable hypothesis.

3.10. Final computation results and discussion

The molecular geometries of ellagic acid, quercetin, and rutin were optimized at the B3LYP level using the DNP basis set, with all electrons explicitly treated, yielding stable, energy-minimized structures suitable for electronic and interfacial analysis. Convergence was confirmed by decreasing SCF energy, small final gradients, and stabilization of optimized coordinates, with final total energies of −1205.97 Ha for ellagic acid, −1169.55 Ha for quercetin, and −2381.81 Ha for rutin. These optimized structures were used to compute HOMO and LUMO orbital energies (Table 10) and the corresponding global reactivity descriptors relevant to adsorption on carbon steel in 1 M HCl. Rutin exhibits the highest HOMO level, indicating the greatest electron-donating capability toward Fe surface centers. Ellagic acid displays the lowest HOMO energy, indicating stronger internal electron localization and more site-specific adsorption. The similar ΔE values indicate comparable inherent stability while retaining sufficient reactivity for surface interaction. Global reactivity descriptors (Electronegativity, χ; Hardness, η; Softness, S, and Electrophilicity, ω) were then derived from the frontier orbitals:

$$\chi = (E_{HOMO}+E_{LUMO})/2,\ \eta = (E_{LUMO}-E_{HOMO})/2,\ S = 1/2\eta,\ \omega = \chi^2/2\eta \quad (17)$$

Ellagic acid, with the highest electrophilicity, favors localized chemisorption at specific Fe sites. Rutin, with the highest HOMO and lowest χ, favors extended surface coverage and hydrogen-bonded film formation. Quercetin spans an intermediate multi-contact binding mode. The COSMO-RS output in Fig. 19 maps how each inhibitor partitions its surface charge across solvent-exposed atoms in 1 M HCl, which in turn governs the way it approaches and organizes on steel in chloride media.

In Fig. 19a, ellagic acid concentrates negative σ density at the carbonyl and phenolic oxygens, with little neutral surface. COSMO-RS therefore predicts short-range, directional contacts to cationic surface sites, for example, $Fe\delta^+$ at defect steps or hydroxo-terminated spots, with limited lateral cohesion. That picture aligns with docking, which prefers chelation motifs via adjacent O atoms and yields compact, low-footprint poses, typically without extended π- π parallel alignment. Because each molecule covers a little area, EIS shows modest surface coverage θ from Rct, moderate Kads, and a ΔGads that is negative but less so than the other molecules. In PDP, this manifests as a smaller icorr decrease at low doses and small Ecorr shifts, indicating a mixed-type action dominated by local blocking. The practical risk, if chloride competes at neighboring vacated sites, is persistent microanodic activity, which matches the patchy protection COSMO-RS implies. Fig. 19b shows quercetin with alternating donor and acceptor σ lobes spread over the aromatic scaffold and a wider neutral belt. COSMO-RS thus supports multi-point anchoring to the surface along with lateral packing through π–π contacts. Docking corroborates this by producing poses that combine O-Fe coordination with near-parallel ring alignment to Fe, increasing footprint without sacrificing binding energy. The result is cooperative growth of a more continuous film. Electrochemically, θ derived from Rct rises faster with concentration than for ellagic acid, Kads increases, and ΔGads becomes more negative. PDP tracks this with a stronger drop in icorr at intermediate concentrations and small, criterion-consistent potential shifts that again indicate mixed-type inhibition. The COSMO neutral segments explain the decrease in Cdl observed in EIS, since compact packing displaces interfacial water and perturbs the double layer. Fig. 19c presents rutin with the broadest σ distribution and the largest fractions of both donor and acceptor surface segments, plus extensive neutral regions contributed by glycosidic hydroxyls and the enlarged envelope. COSMO-RS predicts a mosaic of strong H-bond donors and acceptors interleaved with neutral patches that favor dispersion and cohesive packing, which naturally leads to cooperative multi-site adsorption and multilayer growth. Docking results are consistent with this picture, typically yielding the best scores for poses that engage multiple O centers, while also stabilizing near-parallel orientations that maximize contact area. This electronic and geometric versatility explains why rutin delivers the steepest rise in θ, the largest K_{ads} and most negative ΔG_{ads} from isotherm fits, the greatest increase in R_{ct} and the largest reduction in C_{dl} in EIS, and the largest early decrease in i_{corr} in PDP. Mechanistically, rutin not only caps isolated hot spots, but it also creates a contiguous barrier that suppresses both anodic dissolution and the cathodic hydrogen evolution pathway by restricting charge transfer and reactant access. Fig. 19d, the comparative σ-profiles, quantifies the narrative above. Ellagic acid shows narrow peaks at high absolute σ that signal localized polarity and explain localized chemisorption and patchy coverage. Quercetin broadens toward the center, indicating a balanced donor–acceptor

Table 10
Frontier Molecular Orbital Energies.

Molecule	E_{HOMO} (eV)	E_{LUMO} (eV)	$\Delta E = E_{LUMO} - E_{HOMO}$ (eV)	χ (eV)	η (eV)	S (eV^{-1})	ω (eV)
Ellagic acid	−5.90	−2.32	3.58	4.11	1.79	0.28	4.72
Quercetin	−5.64	−2.08	3.56	3.86	1.78	0.28	4.19
Rutin	−5.41	−1.79	3.62	3.60	1.81	0.28	3.58

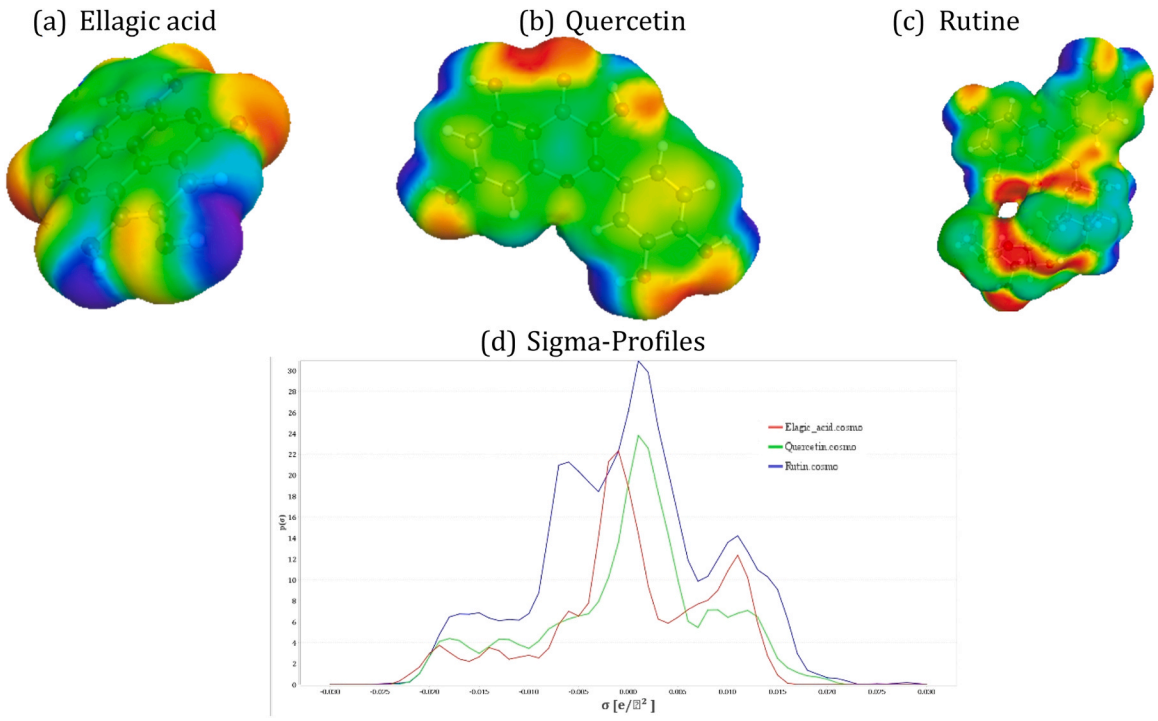

Fig. 19. COSMO-RS polarity maps and σ-profiles.

character that enables multi-point anchoring and better lateral cohesion. Rutin spans the widest σ range with the largest integrated donor and acceptor areas and the most substantial near-neutral plateau, which is exactly the polarity signature of a molecule that can both bind strongly and pack densely. Taken together, COSMO-RS and docking account for the full electrochemical hierarchy. Ellagic acid provides localized chemisorption and moderate protection; quercetin provides multi-point adsorption and continuous monolayer formation; and rutin provides cooperative adsorption and multilayer barrier formation that displaces water and chloride and suppresses both partial reactions.

4. Conclusion

The methanolic fruit extract of *Moringa oleifera* showed strong potential as a green corrosion inhibitor for carbon steel in 1 M HCl, with inhibition efficiency approaching 90% at 20 mg/L. Gravimetric, PDP, and EIS data were mutually consistent and demonstrated that the extract acts as a mixed-type inhibitor through adsorption at the steel-solution interface. The adsorption behavior followed the Langmuir isotherm, while AFM, optical microscopy, and UV-Vis results supported the formation of a compact protective film and the involvement of inhibitor-iron interactions. HPLC-DAD and phytochemical screening indicated that polyphenolic constituents are the main active components. Computational analyses, particularly DFT and COSMO-RS, provided insight into the electronic and polarity characteristics of these molecules, which are relevant to their interaction propensity with metallic surfaces. Among the tentatively identified compounds, rutin, quercetin, and ellagic acid appear to be the most relevant contributors to the protective effect. Molecular docking studies further supported the antioxidant potential of the major phytochemicals identified in the extract. However, these calculations were used solely to investigate ligand interactions with selected biological targets and were not intended to model adsorption on the metal surface. The corrosion inhibition mechanism was established through electrochemical measurements, adsorption studies, surface characterization, and quantum chemical calculations. Overall, the study provides a coherent experimental and theoretical basis for considering *Moringa oleifera* fruit extract as a promising low-dose alternative to conventional synthetic inhibitors. Future work should focus on standardizing the extract composition, isolating the dominant active constituents, and validating the proposed mechanism under broader corrosion conditions.

CRediT authorship contribution statement

Samra Amamra: Writing – original draft, Visualization, Validation, Methodology, Investigation, Formal analysis, Data curation, Conceptualization. **Ilhem Kaabi:** Writing – original draft, Visualization, Validation, Methodology, Investigation, Formal analysis, Data curation, Conceptualization. **Hamza Behloul:** Formal analysis, Validation, Visualization, Investigation, Data curation. **Naouel Boussoualim:** Formal analysis, Data curation, Investigation, Validation, Visualization. **Farida Belkhiri:** Formal analysis, Data curation, Validation, Visualization, Investigation. **Khalil Kaouane:** Formal analysis, Investigation, Validation, Visualization. **Hamza Kemchache:** Data curation, Formal analysis, Investigation, Validation, Visualization. **Abdul Ahad:** Writing – review & editing, Visualization, Validation, Methodology. **Byong-Hun Jeon:** Writing – review & editing, Visualization, Validation, Resources, Investigation, Funding acquisition. **Hyun-Jo Ahn:** Resources, Funding acquisition, Writing – review & editing. **Yacine Benguerba:** Writing – review & editing, Visualization, Validation, Supervision, Software, Resources, Project administration, Methodology, Investigation, Funding acquisition, Formal analysis, Data curation, Conceptualization.

Declaration of Competing Interest

The authors declare that they have no known competing financial interests or personal relationships that could have appeared to influence the work reported in this paper.

Acknowledgments

The authors sincerely thank the Ministry of Higher Education and Scientific Research, Setif 1 University - Ferhat Abbas, and the University Mohamed El Bachir El-Ibrahimi, Bordj Bou Arreridj, as well as the

Directorate General for Scientific Research and Technological Development (DGRSDT), Algeria, for their financial support. They also acknowledge the Mid-Career Research Program (Grant No. RS-2025–00520940) of the Ministry of Education and the Government of the Republic of Korea. The authors further extend their sincere appreciation to the Ongoing Research Funding Program (ORF-2026–959), King Saud University, Riyadh, Saudi Arabia.

Data availability

No data was used for the research described in the article.

References

[1] G.H. Koch, M.P.H. Brongers, N.G. Thompson, Y.P. Virmani, J.H. Payer, International Measures of Prevention, Application, and Economics of Corrosion Technologies Study, NACE International, Houston, TX, USA, 2016.
[2] A. Zarrouk, H. Zarrok, R. Salghi, B. Hammouti, F. Bentiss, R. Touir, M. Bouachrine, Evaluation of N-containing organic compounds as corrosion inhibitors for carbon steel in phosphoric acid, J. Mater. Environ. Sci. 4 (2013) 177–192.
[3] G. Avci, Inhibitor effect of N, N′-methylenediacrylamide on corrosion behavior of mild steel in 0.5 M HCl, Mater. Chem. Phys. 112 (2008) 234–238.
[4] H. Zarrok, H. Oudda, A. Zarrouk, R. Salghi, B. Hammouti, M. Bouachrine, Weight loss measurement and theoretical study of a new pyridazine compound as corrosion inhibitor for C38 steel in hydrochloric acid solution, Der Pharma Chem. 3 (2011) 576–590.
[5] H. Zarrok, R. Salghi, A. Zarrouk, B. Hammouti, H. Oudda, L. Bazzi, L. Bammou, S. S. Al-Deyab, Investigation of the inhibition effect of N-1-naphthylethylenediamine dihydrochloride monomethanolate on the C38 steel corrosion in 0.5 M H2SO4, Der Pharma Chem. (4) (2012) 407–416.
[6] H. Zarrok, H. Oudda, A. El Midaoui, A. Zarrouk, B. Hammouti, M. Ebn Touhami, A. Attayibat, S. Radi, R. Touzani, Some new bipyrazole derivatives as corrosion inhibitors for C38 steel in acidic medium, Res. Chem. Intermed. 38 (2012) 2051–2063.
[7] D.B. Hmamou, M.R. Aouad, R. Salghi, A. Zarrouk, M. Assouag, O. Benali, M. Messali, H. Zarrok, B. Hammouti, Inhibiting effects of 4,5-diphenyl-1H-imidazole-2-thiol for C38 steel in 1 M HCl: electrochemical study, J. Chem. Pharm. Res. 4 (2012) 3489–3497.
[8] H. Zarrok, A. Zarrouk, R. Salghi, Y. Ramli, B. Hammouti, M. Assouag, E.M. Essassi, H. Oudda, M. Taleb, 3,7-Dimethylquinoxalin-2-(1H)-one for inhibition of acid corrosion of carbon steel, J. Chem. Pharm. Res. 4 (2012) 5048–5055.
[9] V.I. Vorobyova, M.I. Skiba, A.S. Shakun, S.V. Nahirniak, Relationship between the inhibition and antioxidant properties of plant and biomass waste extracts, a review, Int. J. Corros. Scale Inhib. 8 (2) (2019) 150–178.
[10] V. Hemapriya, M. Prabakaran, S. Chitra, M. Swathika, S.-H. Kim, I.-M. Chung, Utilization of biowaste as an eco-friendly biodegradable corrosion inhibitor for mild steel in 1 mol/L HCl solution, Arab. J. Chem. 13 (12) (2020) 8684–8696, https://doi.org/10.1016/j.arabjc.2020.09.060.
[11] H. Mobtaker, M. Azadi, M. Rassouli, The corrosion inhibition of carbon steel in 1 M HCl solution by Oestrus ovis larvae extract as a new bio-inhibitor, Heliyon 8 (2022) e12297.
[12] M. Sheydae, The use of plant extracts as green corrosion inhibitors: a review, Surfaces 7 (2024) 380–403.
[13] A. Royani, Moringa oleifera Extract as a Green Corrosion Inhibitor for API 5L in Seawater Medium: Electrochemistry and Surface Study, J. Bio- Tribo-Corros. 12 (2) (2026), https://doi.org/10.1007/s40735-026-01144-7.
[14] S. Benidir, N.E.H. Sobhi, Sustainable corrosion inhibition of carbon steel in 3.5% NaCl using *Moringa oleifera* leaf extract, Electrochemistry 37 (1) (2026), https://doi.org/10.6001/chemija.2026.37.1.5.
[15] A.E.S. Fouda, F. El-Dossoki, M.F. Atia, F.M. Abd El Aziz, A. El-Hossiany, Contribution to the corrosion inhibition of aluminum by aqueous extract of Moringa oleifera in 2 M HCl, Discov. Chem. Eng. 5 (2025) 1, https://doi.org/10.1007/s43938-025-00074-z.
[16] R.T. Vashi, Moringa oleifera as an Eco-friendly Corrosion Inhibitor for Protection of Metals and Alloys-A Review, J. Mater. Environ. Sci. 16 (6) (2025) 1008–1028. http://www.jmaterenvironsci.com.
[17] H. Didouh, M. Sadou, R.K. Suleiman, M. Hadj Meliani, Effect of Combining *Moringa oleifera* and Datura stramonium Extracts as a Green Corrosion Inhibitor for Mild Steel, Corros. Sci. Technol. 24 (2) (2025) 63–75, https://doi.org/10.14773/cst.2025.24.2.63.
[18] H. Didouh, A. Buyuksagis, M. Haddj Meliani, M. Dilek, Y. Kayali, R.K. Suleiman, T. A. Saleh, Investigating the use of Moringa oleifera leaf extract as an environment-friendly corrosion inhibitor for API 5L X52 steel in 1 M HCl, J. Mol. Liq. 390 (2023), https://doi.org/10.1016/j.molliq.2023.122910.
[19] J. Bruneton. Pharmacognosy, phytochemistry, medicinal plants, second ed., Tec & Doc-Lavoisier, Paris, 1993.
[20] K.R. Markham, Techniques of Flavonoid Identification, Academic Press, London, 1982, p. 113.
[21] H.-B. Li, K.-W. Cheng, C.-C. Wong, K.-W. Fan, F. Chen, Y. Jiang, Evaluation of antioxidant capacity and total phenolic content of different fractions of selected microalgae, Food Chem. 102 (3) (2007) 771–776.
[22] T. Bahorun, B. Gressier, F. Trotin, C. Brunete, T. Dine, J. Vasseur, J.-C. Gazin, M. Pinkas, M. Luycky, M. Gazin, Oxygen species scavenging activity of phenolic extract from hawthorn fresh plant organs and pharmaceutical preparations, Arzneim. Forsch. 46 (11) (1996) 1086–1089.
[23] K. Shimada, K. Fujikawa, K. Yahara, T. Nakamura, Antioxidative properties of xanthan on the autoxidation of soybean oil in cyclodextrin emulsion, J. Agric. Food Chem. 40 (1992) 945–948.
[24] J. Yang, J. Guo, J. Yuan, vitro antioxidant properties of rutin, LWT - Food Sci. Technol. 41 (6) (2008) 1060–1066.
[25] K. Le, F. Chiu, K. Ng, Identification and quantification of antioxidants in Fructus lycii, Food Chem. 105 (1) (2007) 353–363.
[26] L.M. Marami, G.M. Dilba, D.A. Babele, E.J. Sarba, A. Gizaw, W.M. Bune, M. D. Bayu, P. Admasu, A. Mekbeb, M. Tadese, K. Abdisa, D. Bayisa, Phytochemical screening and in vitro evaluation of antibacterial activities of Echinops amplexicaulis, Ruta chalepensis, and Salix subserrata against selected pathogenic bacterial strains in West Shewa Zone, Ethiopia, J. Exp. Pharmacol. 13 (2021) 511–520, https://doi.org/10.2147/JEP.S305936.
[27] A. Iguchi, R. Osawa, J. Kawano, A. Shimizu, J. Terajima, H. Watanabe, Effects of repeated subculturing and prolonged storage at room temperature of enterohemorrhagic Escherichia coli O157:H7 on pulsed-field gel electrophoresis profiles, J. Clin. Microbiol. 40 (8) (2002) 3079–3081, https://doi.org/10.1128/JCM.40.8.3079-3081.2002.
[28] M. Hombach, F.P. Maurer, T. Pfiffner, E.C. Böttger, R. Furrer, Standardization of operator-dependent variables affecting precision and accuracy of the disk diffusion method for antibiotic susceptibility testing, J. Clin. Microbiol. 53 (12) (2015) 3864–3869, https://doi.org/10.1128/JCM.02351-15.
[29] S. Rana, S. Dixit, A. Mittal, silico target identification and validation for antioxidant and anti-inflammatory activity of selective phytochemicals, Braz. Arch. Biol. Technol. 62 (2019) e19190048, https://doi.org/10.1590/1678-4324-2019190048.
[30] Z.D. Benyahlou, F.T. Baara, S. Yahiaoui, Y. Megrouss, N. Boukabcha, A. Djafri, A. Chouaih, A. Hatzidimitriou, Synthesis, crystal structure, Hirshfeld surface, energy framework, NCI-RDG, theoretical calculations, and molecular docking of (*Z*)-4,4′-bis[-3-N-ethyl-2-N′-(phenylimino)thiazolidin-4-one] methane, J. Mol. Struct. 1277 (2023) 134781, https://doi.org/10.1016/j.molstruc.2022.134781.
[31] B.H. Hijazi, A. Rammal, H. Hachem, A. Saad, Z. Badran, Techniques for the extraction of bioactive compounds from Lebanese Urtica dioica, Am. J. Phytomedicine Clin. Ther. 1 (6) (2013) 507–513.
[32] A.M. Gómez-Caravaca, M. Gómez-Romero, D. Arráez-Román, A. Segura-Carretero, A. Fernández-Gutiérrez, Advances in the analysis of phenolic compounds in products derived from bees, J. Pharm. Biomed. Anal. 41 (2006) 1220–1234.
[33] A. Podsedek, Natural antioxidants and antioxidant capacity of Brassica vegetables, a review, LWT - Food Sci. Technol. 40 (2007) 1–11.
[34] A.A. Mariod, M.I. Ramlah, I. Norsharina, Antioxidant activities of phenolic-rich fractions obtained from black mahlab (Monechma ciliatum) and white mahlab (Prunus mahaleb) seedcakes, Food Chem. 118 (2010) 120–127.
[35] S. Athamena, I. Chalghem, A. Kassah-Laouar, S. Laroui, S. Khebri, Activité antioxydante et antimicrobienne d'extraits de Cuminum cyminum L, Leban. Sci. J. 11 (1) (2010) 69–81.
[36] K.E. Heim, A.R. Tagliaferro, D.J. Bobilya, Flavonoid antioxidants, chemistry, metabolism, and structure-activity relationships, J. Nutr. Biochem. 13 (2002) 572–584.
[37] A. Torres de Pinedo, P. Peñalver, J.C. Morales, Synthesis and evaluation of new phenolic-based antioxidants, structure-activity relationship, Food Chem. 103 (2007) 55–61.
[38] C. Popovici, I. Saykova, B. Tylkowski, Évaluation de l'activité antioxydante des composés phénoliques par la réactivité avec le radical libre DPPH, Rev. De. Génie Ind. 4 (2010) 1–8.
[39] A. Rodríguez-Bernaldo de Quirós, P.A. Frecha, J. Vidal, J. López-Hernández, Antioxidant compounds in edible brown seaweeds, Eur. Food Res. Technol. 231 (3) (2010) 495–498.
[40] R.S. Rajasree, S.P. Ittiyavirah, P.P. Naseef, M.S. Kuruniyan, G.S. Anisree, M. Elayadeth-Meethal, An evaluation of the antioxidant activity of a methanolic extract of Cucumis melo L. fruit (F1 hybrid), Separations 8 (8) (2021) 123.
[41] B. Pradhan, S. Patra, S.R. Dash, R. Nayak, C. Behera, M. Jena, Evaluation of the antibacterial activity of methanolic extract of Chlorella vulgaris Beyerinck with special reference to antioxidant modulation, Future J. Pharm. Sci. 7 (2021) 1–11.
[42] S.J. Dixon, B.R. Stockwell, The role of iron and reactive oxygen species in cell death, Nat. Chem. Biol. 10 (1) (2014) 9–17, https://doi.org/10.1038/nchembio.1416.
[43] M.M. Solomon, S.A. Umoren, M.A. Quraishi, M. Salman, Myristic acid-based imidazoline derivative as effective corrosion inhibitor for steel in 15% HCl medium, J. Colloid Interface Sci. 551 (2019) 47–60.
[44] M.M. Solomon, S.A. Umoren, M.A. Quraishi, D.B. Tripathy, E.J. Abai, Effect of alkyl chain length, flow, and temperature on the corrosion inhibition of carbon steel in a simulated acidizing environment by an imidazoline-based inhibitor, J. Pet. Sci. Eng. 187 (2020) 106801.
[45] Riggs, O.L., Jr. Corrosion Inhibitors, 2nd ed.; Nathan, C.C.: Houston, TX, 1973.
[46] B. Zerouni, I. Kaabi, M. Al-Noaimi, S. Amamra, T. Douadi, M.R. Khelladi, I. Lakikza, S.I. Aouni, A. Boublia, N. Chafai, Y. Benguerba, Hydrazonamide-derived Schiff bases as corrosion inhibitors for XC48 steel in acidic media and potent antioxidants: experimental and theoretical insights, J. Ind. Eng. Chem. 156 (2026) 666–698, https://doi.org/10.1016/j.jiec.2025.09.013.
[47] I. Kaabi, T. Douadi, D. Daoud, S. Issaadi, L. Sibous, S. Chafaa, Synthesis, characterization, and anticorrosion properties of two new Schiff bases derived from

diamino diphenyl ether on carbon steel X48 in 1 M HCl, J. Adhes. Sci. Technol. 35 (6) (2021) 559–589, https://doi.org/10.1080/01694243.2020.1816777.
[48] S. Amamra, I. Kaabi, L. Arrar, A. Baghiani, M. Hamla, S.I. Aouni, I. Lakikza, A. Boublia, B. Ernst, M. Raish, Y. Benguerba, Thymus vulgaris extract: a green approach to antioxidant efficacy, antibacterial action and corrosion inhibition, J. Environ. Chem. Eng. 13 (2025) 116067, https://doi.org/10.1016/j.jece.2025.116067.
[49] J. Aljourani, K. Raeissi, M.A. Golozar, Benzimidazole and its derivatives as corrosion inhibitors for mild steel in 1 M HCl solution, Corros. Sci. 51 (2009) 1836–1843, https://doi.org/10.1016/j.corsci.2009.05.011.
[50] L. Raisemche, I. Kaabi, T. Douadi, M. Al-Noaimi, A. Alrashed, M.S. Mubarak, N. Elboughdiri, A. Zouaoui, Y. Benguerba, Corrosion inhibition of mild steel in acidic environments, mechanistic insights and protective effects of azo-cum inhibitor, J. Environ. Chem. Eng. 12 (2024) 112354.
[51] M. Said-Ahmed, M. Lebrini, Alkaloid extract from Chimarrhis cymosa as a corrosion inhibitor for C38 steel in 1 M hydrochloric acid, electrochemical and XPS studies, Metals 15 (2025) 523, https://doi.org/10.3390/met15050523.
[52] F.B. Growcock, R.J. Jasinski, Time-resolved impedance spectroscopy of mild steel in concentrated hydrochloric acid, J. Electrochem. Soc. 136 (1989) 2310–2314.
[53] P. Li, J.Y. Lin, K.L. Tan, J.Y. Lee, Electrochemical impedance and X-ray photoelectron spectroscopic studies of the inhibition of mild steel corrosion in acids by cyclohexylamine, Electrochim. Acta 42 (1997) 605–615.
[54] Z. Stoynov, Impedance modelling and data processing, structural and parametrical estimation, Electrochim. Acta 35 (1990) 1493–1499.
[55] J.R. Macdonald, Impedance spectroscopy and its use in analyzing the steady-state AC response of solid and liquid electrolytes, J. Electroanal. Chem. 223 (1987) 25–50.
[56] S. Zhang, Z. Tao, W. Li, B. Hou, The effect of some triazole derivatives as inhibitors for the corrosion of mild steel in 1 M hydrochloric acid, Appl. Surf. Sci. 255 (15) (2009) 6757–6763, https://doi.org/10.1016/j.apsusc.2008.09.089.
[57] A.M. Abuelela, M.A. Bedair, W.M. Zoghaib, L.D. Wilson, T.A. Mohamed, Molecular structure and mild steel/HCl corrosion inhibition of 4,5-dicyanoimidazole, vibrational, electrochemical, and quantum mechanical calculations, J. Mol. Struct. 1230 (2021) 129647, https://doi.org/10.1016/j.molstruc.2020.129647.
[58] M.A. Bedair, A novel coumarin-azo Schiff base for dual corrosion inhibition for steel in acidic environments and anti-SRB protection, experimental and computational insights, Results Surf. Interfaces 19 (2025) 100511, https://doi.org/10.1016/j.rsurfi.2025.100511.
[59] N. Elboughdiri, I. Lakikza, A. Boublia, S.I. Aouni, N.E.H. Hammoudi, J. Georgin, D. S.P. Franco, H. Ferkous, D. Ghernaout, Y. Benguerba, Application of statistical physical, DFT computation, and molecular dynamics simulation for enhanced removal of crystal violet and basic fuchsin dyes utilizing biosorbent derived from residual watermelon seeds (Citrullus lanatus), Process. Saf. Environ. Prot. 186 (2024) 995–1010, https://doi.org/10.1016/j.psep.2024.03.093.
[60] S.E.I. Lebouachera, O. Balamane-Zizi, A. Boublia, M.A. Ghriga, M. Hasanzadeh, H. El Hadri, et al., Understanding the factors affecting the adsorption of surface-active agents onto reservoir rock in chemical-enhanced oil recovery applications: a comprehensive review, Chem. Afr. 7 (2024) 2283–2306, https://doi.org/10.1007/s42250-024-00931-4.
[61] M. Azzouzi, W. Daoudi, O. Dagdag, A. Berisha, H. Kim, A. Oussaid, A. El Aatiaoui, A. Oussaid, Corrosion inhibition and in silico toxicity assessment of imidazo[1.2-a] pyrimidine-Schiff base derivatives as effective and environmentally friendly corrosion inhibitors for mild steel, RSC Adv. 15 (2025) 12342.
[62] D. Karra, N. Timoudan, D.R. Bazanov, N.A. Lozinskaya, H. Zarrok, H. Oudda, Benmessaoud Left, D. Zertoubi, M. Assouag, M. Benhiba, F. El Faydy, M. Saranya, J. Abuelizz, H.A. Zarrouk, A. Corrosion inhibition performance of imidazole derivative for protection of carbon steel in hydrochloric acid solution, experimental and theoretical analysis, Int. J. Electrochem. Sci. 20 (2025) 101015, https://doi.org/10.1016/j.ijoes.2025.101015.
[63] B. Tan, J. He, S. Zhang, C. Xu, S. Chen, H. Liu, W. Li, Insight into anticorrosion nature of betel leaves water extracts as the novel and eco-friendly inhibitors, J. Colloid Interface Sci. 585 (2021) 287–301.
[64] Q. Wang, B. Tan, H. Bao, Y. Xie, Y. Mou, P. Li, D. Chen, Y. Shi, X. Li, W. Yang, Evaluation of Ficus tikoua leaves extract as an eco-friendly corrosion inhibitor for carbon steel in HCl media, Bioelectrochemistry 128 (2019) 49–55.
[65] A. Dehghani, G. Bahlakeh, B. Ramezanzadeh, M. Ramezanzadeh, Experimental complemented with microscopic (electronic/atomic)-level modeling explorations of Laurus nobilis extract as green inhibitor for carbon steel in acidic solution, J. Ind. Eng. Chem. 84 (2020) 52–71.
[66] S. Amamra, I. Kaabi, O.E. Belhaddad, A. Baghiani, L. Arrar, Phenolics composition, antioxidant and corrosion inhibition efficiency, capacity of Fraxinus excelsior extracts, J. Chil. Chem. Soc. 66 (3) (2021) 5262–5267, https://doi.org/10.4067/S0717-97072021000305262.
[67] M. Benahmed, I. Selatnia, N. Djeddi, S. Akkal, H.J. Laouer, Adsorption and corrosion inhibition properties of butanolic extract of Elaeoselinum thapsioides and its synergistic effect with Reutera lutea (Desf.) Maire (Apiaceae) on A283 carbon steel in hydrochloric acid solution, Chem. Afr. 3 (2020) 251–261.
[68] M.A. El-Hashemy, A.M. Almehmadi, Evaluation of Glebionis coronaria L. flower extract as a novel green inhibitor for mild steel corrosion in acidic environment, Biomass. Convers. Biorefinery 15 (2025) 1121–1137, https://doi.org/10.1007/s13399-024-05344-4.
[69] Y.-C. Cheng, W.H. Prusoff, Relationship between the inhibition constant (Ki) and the concentration of inhibitor which causes 50 % inhibition (I50) of an enzymatic reaction, Biochem. Pharmacol. 22 (1973) 3099–3108, https://doi.org/10.1016/0006-2952(73)90196-2.
[70] F. Belkhadem, F.T. Brahimi, Z.D. Benyahlou, S. Yahiaoui, B. Trari, A.A. Othman, Synthesis, pharmacological evaluation, and molecular docking studies of some 1,3,4-oxadiazolyl-5-yl thiones bearing halo-nitrophenyl hydrazide derivatives as antioxidant and antimicrobial agents—Journal, Mol. Struct. 1329 (2025) 141389.